REPORT DOCUMENTATION PAGE

Form Approved
OMB No. 0704-0188

1. AGENCY USE ONLY (Leave blank)	2. REPORT DATE	3. REPORT TYPE AND DATES COVERED
	March 95	final 15Dec91 - 14JAN95

4. TITLE AND SUBTITLE
An Analysis of Wake-Stator Interaction in Airfoil Cascades

5. FUNDING NUMBERS
F49620-92-C-0017

6. AUTHOR(S)
M. Barnett, D.L. Sondak

7. PERFORMING ORGANIZATION NAME(S) AND ADDRESS(ES)
United Technologies Research Center

8. PERFORMING ORGANIZATION REPORT NUMBER
AFOSR-TR-95-0266

9. SPONSORING/MONITORING AGENCY NAME(S) AND ADDRESS(ES)
Air Force Office Of Scientific Research
Aerospace & Materials Sciences Directorate
110 Duncan Avenue, Suite B-115
Bolling AFB DC 20332-0001
NA

10. SPONSORING/MONITORII AGENCY REPORT NUMBE

11. SUPPLEMENTARY NOTES

12a. DISTRIBUTION/AVAILABILITY STATEMENT
APPROVED FOR PUBLIC RELEASE
DISTRIBUTION IS UNLIMITED

12b. DISTRIBUTION CODE

13. ABSTRACT *(Maximum 200 words)*

A computational study has been conducted in order to provide insight into the details of the unsteady flow in the leading-edge region of airfoil cascades during wake-stator interaction. The calculations are performed at off-design operating conditions, since the flow at conditions near to those at which stall onset occurs is of particular interest in helping to understand the mechanisms responsible for compressor stall. A thorough understanding of these mechanisms will provide the underpinnings needed to design compressors with favorable stall characteristics, using fewer design iterations than are typical with the present state of the art. The results obtained during this study show that the use of highly refined grids leads to the resolution of complex unsteady phenomena associated with wake-stator interaction. The structure of the interaction is shown to change significantly as the magnitude of the wake deficit is increased, with shedding from the leading-edge separation bubble suppressed compared to that observed for the cases with small wake deficit or no wake disturbance.

14. SUBJECT TERMS	15. NUMBER OF PAGES
Airfoil, Cascades, Wake, Stator	40
DTIC QUALITY INSPECTED 5	16. PRICE CODE

17. SECURITY CLASSIFICATION OF REPORT	18. SECURITY CLASSIFICATION OF THIS PAGE	19. SECURITY CLASSIFICATION OF ABSTRACT	20. LIMITATION OF ABSTRACT

An Analysis of Wake-Stator Interaction in Airfoil Cascades

Contents

An Analysis of Wake-Stator
Interaction in Airfoil Cascades

Summary

A computational study has been conducted in order to provide insight into the details of the unsteady flow in the leading-edge region of airfoil cascades during wake-stator interaction. The calculations are performed at off-design operating conditions, since the flow at conditions near to those at which stall onset occurs is of particular interest in helping to understand the mechanisms responsible for compressor stall. A thorough understanding of these mechanisms will provide the underpinnings needed to design compressors with favorable stall characteristics, using fewer design iterations than are typical with the present state of the art. The results obtained during this study show that the use of highly refined grids leads to the resolution of complex unsteady phenomena associated with wake-stator interaction. The structure of the interaction is shown to change significantly as the magnitude of the wake deficit is increased, with shedding from the leading-edge separation bubble suppressed compared to that observed for the cases with small wake deficit or no wake disturbance.

1. Introduction

Turbomachinery components such as turbines and compressors are characterized by the presence of circumferentially nonuniform flow due to nonaxisymmetric disturbances at the inlet and exit of the components, and due to wakes and potential-flow effects of the individual blades within each blade row of the turbine and compressor. The relative motion of the stator and rotor blade rows produces periodic interactions between adjacent blade rows resulting in unsteadiness within the flow field. The unsteadiness within turbines and compressors affects their performance, stability and durability; the latter two are related to the "operability" of the engine.

The problem at the focus of this effort is the breakdown of the suction-surface boundary layer on compressor stator blades caused by the unsteady interaction with wakes from the upstream rotor, and the subsequent near-term evolution of the vortical structures that erupt from the boundary layer during its breakdown. For the particular cases considered herein the compressor cascade is operating, in the absence of the upstream wakes (which will be referred to hereafter as the "*undisturbed*" condition), at an *off-design* incidence condition for which the flow is separated. At the undisturbed condition small-scale unsteadiness associated with the separation bubble is observed. However, this unsteady effect is smaller than that associated with the wake passing. Furthermore, the Reynolds number, $Re = \rho_1 V_1 C/\mu_1$, where the subscript "1" denotes the circumferentially-averaged value from the steady *baseline* solution (i.e., the solution obtained in the absence of upstream wakes), is assumed to be small enough that the flow can be taken to be laminar in the neighborhood of the suction-surface leading edge for the purpose of this investigation. This assumption is made in order to reduce the uncertainties associated with turbulence modeling as much as possible. Transition is imposed downstream of the neighborhood of interest, in the vicinity of the suction-surface leading-edge and near the leading edge of the pressure surface; it is believed that this will have a negligible effect on the local wake/boundary-layer interactions calculated as part of this study. We recognize that the effect of the rotor wakes on transition can be quite significant, as discussed in the work of Hodson [1], for example. However, because the principal intent of this study is to examine the local flow behavior associated with the interaction of the wake with the suction-surface boundary layer at off-design conditions, and issues associated with transition are beyond the scope of this investigation, the simple assumption of a fixed transition location is made.

The wake-stator interaction is modeled herein within the context of a single blade-row analysis by introducing a simulated wake at the upstream boundary of the computational domain containing a single stator airfoil. This approach neglects the potential effect associated with the pressure disturbances of the adjacent rotor blades that are moving with respect to the stator blade row. Since the focus of this study is on the interaction of the wake with the stator boundary-layer, the present approach remains consistent despite this. The inlet wake profile is translated in the circumferential direction, simulating the motion of an upstream rotor in the frame of reference of the stator. The wake is convected downstream at the local flow velocity, impinging on the leading edge and washing over the stator suction- and pressure-surface boundary layers. Once the wake enters the blade passage it migrates away from the suction surface towards the pressure surface, a phenomena which is due to

the excess of circumferential velocity within the wake [2]. As this high vorticity fluid passes over the leading-edge region it can induce an eruption of vorticity from the suction-surface boundary layer, which is susceptible to breakdown in the region of adverse pressure gradient near the blade leading edge.

The focus of the present investigation is on the aforementioned wake/boundary-layer interaction occurring on stators operating at off-design conditions, and particularly on the mechanisms associated with the interaction of the wake with the suction-surface boundary layer in the leading-edge region, where an adverse pressure gradient exists. Therefore, it is not the intent of this effort to study the evolution of the flow within the stator passage after the initial eruption phase, although this is an interesting problem, as shown in the studies by Valkov [3] and Valkov and Tan [4], for example. In those references the authors examined the details of the interaction of the rotor wakes with the stator boundary layer. However, in contrast to the present study, they did not attempt to resolve the small-scale structure of boundary layer during the interaction, but focused more on the overall structural evolution of the flow features. In the report of Valkov [3] the wake-stator interaction was investigated under a variety of conditions, including the effects of variations in incidence, Reynolds number and wake velocity deficit.

Because the local structure of unsteady wake/boundary-layer interaction phenomena are the focus of this investigation, it will be assumed that the choice of rotor-stator blade ratio will not significantly alter the qualitative behavior of the interaction, allowing us to limit the calculations to a single blade passage, significantly reducing the computational effort required relative to multiple-passage calculations. One consequence of this, however, is that the interaction between the wakes and the stators produces a disturbance (i.e., a "response") that propogates upstream without decay (in theory, though not necessarily in computations), and influences the incoming wakes. This issue will be discussed further in the Results section. Finally, it is assumed that the flow is two-dimensional in order to keep the scope of the problem manageable in terms of the resources required to perform the numerical simulations.

The problem considered herein is similar in some ways to that studied by Peridier, et al [5,6], who considered the eruption of vorticity from a flat-plate boundary layer over which a vortex is convected. There is also a relationship between the present problem and that investigated by Reisenthal, et al [7,8], who considered the model problem of a stationary, two-dimensional airfoil at non-zero angle of attack for which a no-slip surface boundary condition was impulsively applied, producing a leading-edge separation. Another study that addressed some issues that are relevant to this investigation is that of Bhaskaran and Rothmayer [9], who considered the onset of unsteady leading-edge separation on pitching and oscillating airfoils. An examination of the papers cited above and other investigations in this general area indicates that, when laminar vortical eruptions occur, many of the local flow features are qualitatively the same, regardless of differences in the nature of the global flow field.

Because this investigation is focused on off-design operating conditions, it is hoped that the results may aid in the ongoing efforts to better understand the detailed mechanisms of stall onset. Stall onset has been the subject of numerous experimental, theoretical, and computational investigations during the last several years, many of which have been focused on isolated airfoil stall associated with helicopter rotors and highly maneuverable flight vehicles. The extensive reviews by Carr [10] and Carr and McCroskey [11], for example, provide an overview of experimental studies that have helped to increase the level of understanding of

stall phenomena, and also include reviews of related theoretical and computational studies. Several recent theoretical studies have shed light on various aspects of stall onset. In particular, asymptotic (Reynolds number, $Re \rightarrow \infty$) analyses (e.g., Refs. 5, 12–14) and finite-Re analyses of stall and related phenomena (e.g., Refs. 6 and 9) have provided important insights into some of the details of stall onset and vortex eruptions on airfoils, have aided in identifying the dominant terms in the governing equations during various stages of stall onset, and have revealed the critical length and time scales as they change during the evolution of the stall vortex from pre-inception to eruption. Doligalski noted, in his recent review of CFD challenges faced in problems of relevance to the U.S. Army [15], that the necessity of resolving the many disparate length and time scales that arise in problems with unsteady separation and/or stall remains a significant hindrance to achieving accurate computational solutions for such problems. Clearly, the identification of the critical length and time scales provided by the relevant theoretical studies is a crucial step towards addressing this issue.

The detailed relationship between the phenomenon of turbomachinery compressor stall, which usually occurs when a compressor is operating at severe off-design conditions, and isolated airfoil stall, which has been the focus of most of the studies cited above, is not clear at the present time. It is known that a dramatic increase in flow losses (due to end wall and/or airfoil separation) in compressors can lead to the loss of overall compression-system stability resulting in either rotating stall or surge. However, due to the complexity of compression-system dynamics, wherein the loss of stability is dependent on several compression-system parameters, the precise connection between boundary-layer separation and/or vortical eruptions and compressor stall/surge is not yet understood in detail. Ultimately, the ability to *control* compressor stall/surge, which would significantly enhance the operability of turbomachinery, will require continuing advances in the understanding of the physical processes associated with stall. The current absence of any widespread use of effective stall-control methods in real-world engineering applications, despite the high potential payoff, supports to the need for further research in this area.

Navier-Stokes CFD analyses have been applied in numerous studies of stall and related phenomena. Some examples can be found in the papers of Choudhuri, et al. [16], Mehta [17], Ghia, et al [18], Visbal [19], and Patterson and Lorber [20]. In addition, the papers of Reisenthel and Childs [7] and Reisenthel [8] are interesting because of their use of a higher-order accurate (eighth-order spatial, third-order temporal) numerical scheme and the very careful attention that was paid to validating the grid convergence properties of their unsteady solutions.

The problem of turbomachinery blade-row interaction has been studied experimentally, theoretically and computationally by numerous investigators over the last two decades. For some examples, see the review paper by Verdon [21] and the papers by Kerrebrock and Mikolajczak [2], Dring et al. [22], Hodson [23], Rai [24], Giles [25], Valkov [3] and Valkov and Tan [4].

2. Physical and Mathematical Models

The physical model in this study considers time-dependent flow, with negligible body forces, of a calorically perfect gas through two-dimensional blade rows. The field equations considered in this investigation are the time-dependent Navier-Stokes equations. The governing equations can be written in non-dimensional form and in terms of body-fitted coordinates as

$$Q_\tau + \left(F_i + Re^{-1}F_v\right)_\xi + \left(G_i + Re^{-1}G_v\right)_\eta = 0 \tag{2.1}$$

where the subscripts i refer to inviscid quantities, the subscripts v refer to viscous quantities, the subscripts ξ and η refer to derivatives with respect to the body-fitted coordinate directions, and Re is the Reynolds number. The vector of conserved variables is

$$Q = J^{-1}\bar{Q} \tag{2.2}$$

and the inviscid flux vectors are

$$F_i = J^{-1}(\xi_t\bar{Q} + \xi_x\bar{F}_i + \xi_y\bar{G}_i) \tag{2.3}$$

$$G_i = J^{-1}(\eta_t\bar{Q} + \eta_x\bar{F}_i + \eta_y\bar{G}_i) \tag{2.4}$$

The Jacobian of the transformation (from physical Cartesian (x, y) to computational curvilinear (ξ, η) coordinates) and the other metric quantities are given by

$$J = x_\xi y_\eta - y_\xi x_\eta \tag{2.5}$$

$$\xi_x = y_\eta/J, \quad \xi_y = -x_\eta/J, \quad \eta_x = -y_\xi/J, \quad \eta_y = x_\xi/J \tag{2.6}$$

In the Cartesian coordinate frame, the conserved variable and inviscid flux vectors are defined as

$$\begin{aligned} \bar{Q} &= [\rho, \rho u, \rho v, e_t]^T \\ \bar{F}_i &= \left[\rho u, \rho u^2 + P, \rho uv, (e_t + P)u\right]^T \\ \bar{G}_i &= \left[\rho v, \rho uv, \rho v^2 + P, (e_t + P)v\right]^T \end{aligned} \tag{2.7}$$

where ρ is the density, u and v are the Cartesian velocity components, P is the thermodynamic pressure, and e_t is the total internal energy.

An eddy viscosity formulation is used to model turbulent phenomena. The effective viscosity and effective thermal conductivity are defined as

$$\mu = \mu_L + \mu_T \qquad \kappa/c_p = \mu_L/Pr_L + \mu_T/Pr_T \tag{2.8}$$

where κ is the thermal conductivity, c_p is the ratio of specific heats, and the subscripts L and T refer to the laminar (molecular) and turbulent (eddy) quantities, respectively. The turbulent viscosity, μ_T, for the surface boundary layers is calculated using the two-layer Baldwin-Lomax algebraic turbulence model [26].

In the present study the location of transition is specified, rather than modeled. In addition to the location at which transition begins, the length of the transition region can be specified as well. In the region between the beginning and end of transition an intermittency function which varies between zero and one is specified according to the model of Dwahan and Narasimha [27].

2.1 Solution Procedure

The numerical procedure for the two-dimensional analysis consists of a time marching, implicit, third-order spatially accurate, second-order temporally accurate, upwind, finite-difference scheme. The inviscid fluxes are discretized according to the scheme developed by Chakravarthy and Osher [28]. The viscous fluxes are calculated using standard central differences. An alternating direction, approximate-factorization technique is used to compute the time rate changes in the primary variables. In addition, Newton sub-iterations can be used at each global time step to increase stability and reduce linearization errors. Further details of the numerical techniques can be found in Refs. 29,30 and 31.

2.2 Grid Generation

The numerical analyses use zonal grids to discretize the turbomachinery flow fields (see Fig. 1). A combination of O- and H-grid sections are generated at constant radial spanwise locations in the blade-to-blade direction extending upstream of the airfoil leading edge to downstream of the airfoil trailing edge. Algebraically generated H-grids are used in the regions upstream of the leading edge, downstream of the trailing edge and in the inter-blade region. The O-grid, which is body-fitted to the surface of the airfoil and generated using an elliptic equation solution procedure, is used to properly resolve the viscous flow in the blade passages and to easily apply the algebraic turbulence model. Computational grid lines within the O-grid are stretched in the blade-normal direction with a fine grid spacing at the wall.

The construction of the algebraically generated H-type grids begins with the calculation of the airfoil mean camberline. The mean camberline is extended upstream of the airfoil leading edge and downstream of the airfoil trailing edge, using decay functions to control the incremental changes in the axial and tangential distances. Half the blade pitch is added to and subtracted from every computational grid point along the extended camberline to form the first and last grid lines in the tangential direction. Computational grid lines are then added at equal increments between the first and last grid lines in the tangential direction.

The generation of the O-type grids begins with the specification of four points on the H-grid which delineate the outer boundary of the O-grid. The "box" which forms the outer boundary of the O-grid is then smoothed to eliminate the discontinuities in the slope at the corner points. The inner boundary of the O-grid is the surface of the airfoil. An initial grid with uniform spacing is generated between the inner and outer boundaries. An elliptic solution procedure, similar to that developed by Sorenson [32], is used to produce a nearly orthogonal grid. The elliptic equations can be written as

$$\alpha x_{\xi\xi} - 2\beta x_{\xi\eta} + \gamma x_{\eta\eta} = -J^2 (P x_\xi + Q x_\eta) \tag{2.9}$$

$$\alpha y_{\xi\xi} - 2\beta y_{\xi\eta} + \gamma y_{\eta\eta} = -J^2 (P y_\xi + Q y_\eta) \tag{2.10}$$

where

$$\alpha = {x_\eta}^2 + {y_\eta}^2 \tag{2.11}$$

$$\beta = x_\xi x_\eta + y_\xi y_\eta \tag{2.12}$$

$$\gamma = {x_\xi}^2 + {y_\xi}^2 \tag{2.13}$$

and P, Q are forcing functions used to control computational grid point clustering and orthogonality near solid walls. Equations (2.9) and (2.10) are solved using a successive line over-relaxation (SLOR) technique. Finally, the grid points are algebraically redistributed near the airfoil surface to resolve viscous layer quantities. Increasing the amount of grid overlap enhances the stability and accuracy of the flow solution, but also increases the number of redundant grid points in the calculation.

A modification was made to the grid generation procedure as part of the current investigation. Because of the need for a very fine streamwise grid in the region of interest the clustering function was modified to allow the location, the streamwise extent and the degree of clustering to be specified by the user.

2.3 Boundary Conditions

The inlet and exit boundary conditions used in the two-dimensional numerical analysis are based on a characteristic analysis of the linearized Euler equations. In the numerical procedure, quasi-two-dimensional characteristic boundary conditions are solved implicitly along with the interior of the computational domain. An explicit update, based on fully two-dimensional boundary conditions, is then used to increase solution accuracy. For viscous flows, it is assumed that the computational inlet and exit are in regions where the flow is predominantly inviscid, and the characteristic boundary conditions are retained. At solid surfaces, a formulation based on the normal momentum equation, no-slip condition, and specified heat transfer or wall temperature condition, is implemented for viscous flows. The boundary conditions are explained in detail in the following sections.

2.3.1 Inlet Boundary Conditions

If the flow entering the computational domain is subsonic, then three characteristic waves (an entropy wave, one pressure wave, and a vorticity wave) are entering the computational domain and must be specified, while a fourth characteristic wave (a second pressure wave) is leaving the computational domain and is calculated as part of the flow solution. Since characteristic waves are sometimes difficult to measure experimentally, they are often replaced by other quantities which resemble their behavior and can be readily measured. In particular, the entropy is often replaced by the total pressure (which simplifies the process of maintaining a given mass flow rate, but can cause substantial pressure reflections), the specified pressure wave is often replaced by the total temperature or a Riemann invariant, and the vorticity wave is often replaced by the inlet flow angle. In the following discussions, several of the alternative specifications are considered.

Implicit Inlet B.C.'s

The boundary conditions in the computational analysis are solved as part of the implicit solution procedure, followed by a post-iteration correction to improve the accuracy of the solution. The following implicit solution procedure extends those developed by Chakravarthy [33] and Rai and Chausee [34]. Consider an approximate factorization scheme, written in semi-

discretized form and utilizing only one Newton iteration

$$[I + \Delta t\,(\partial_\xi A)]\,[I + \Delta t\,(\partial_\eta B)]\,\Delta Q = -\Delta t\,(\partial_\xi F + \partial_\eta G) \tag{2.14}$$

where A and B are the fluid dynamic Jacobian matrices. Equation 2.14 can be solved by the following procedure:

- Determine the residual as

$$\Delta Q^* = -\Delta t\,(\partial_\xi F + \partial_\eta G) \tag{2.15}$$

- Make a solution sweep parallel to the inlet boundary

$$[I + \Delta t\,(\partial_\eta B)]\,\Delta Q^{**} = \Delta Q^* \tag{2.16}$$

- Make a solution sweep normal to the inlet boundary

$$[I + \Delta t\,(\partial_\xi A)]\,\Delta Q = \Delta Q^{**} \tag{2.17}$$

At the inlet boundary, the first two steps of this procedure are unchanged. The boundary conditions are not enforced until the third step of the procedure. The boundary procedure begins with the symbolic transformation of the governing equations into characteristic form by premultiplying by the left eigenvectors, $T_\xi{}^{-1}$, of the A matrix

$$T_\xi{}^{-1}\,[I + \Delta t\,(\partial_\xi A)]\,\Delta Q = T_\xi{}^{-1}\Delta Q^{**} \tag{2.18}$$

Next, the equations of motion in characteristic form are premultiplied by a selection matrix, which accounts for only the characteristic information which is leaving the computational domain. For subsonic inflow the information associated with the upstream propagating pressure wave leaves the computational domain, so the selection matrix becomes

$$L_i = \begin{bmatrix} 0 & 0 & 0 & 0 \\ 0 & 0 & 0 & 0 \\ 0 & 0 & 0 & 0 \\ 0 & 0 & 0 & 1 \end{bmatrix} \tag{2.19}$$

and

$$\left[L_i T_\xi{}^{-1} I + L_i T_\xi{}^{-1}\Delta t\,(\partial_\xi A)\right]\,\Delta Q = L_i T_\xi{}^{-1}\Delta Q^{**} \tag{2.20}$$

The technique used to determine the boundary fluxes on the right-hand side of Eqn. (2.20) is different than that used in the interior of the computational domain. At the boundary, the fluxes in the η computational direction are calculated in the same manner as in the interior of the computational domain, using Osher's scheme. The fluxes in the ξ direction are calculated using second-order accurate one-sided differences. Thus, the fluxes at the boundary are third-order accurate in the η direction, but only second-order accurate in the ξ direction.

The boundary conditions corresponding to the positive eigenvalues are then symbolically combined with the equations of motion as

$$\left[C + L_i T_\xi{}^{-1} I + L_i T_\xi{}^{-1}\Delta t\,(\partial_\xi A)\right]\,\Delta Q = L_i T_\xi{}^{-1}\Delta Q^{**} + \left(\Phi_i{}^{n+1} - \Phi_i{}^{n}\right) \tag{2.21}$$

where $C = \partial\Phi_i/\partial Q$ is the Jacobian of the boundary variables with respect to the dependent variables, and Φ is the vector containing the boundary variables given by

$$\Phi_i = \begin{bmatrix} s \\ RT_t \ \ (R^+) \\ v \ \ (\beta) \\ 0 \end{bmatrix} \tag{2.22}$$

The variables in parentheses indicate the alternative characteristic variables discussed above. The zero in the fourth row corresponds to the only non-zero entry of the inlet selection matrix and indicates information that is determined by the equations of motion. The forcing function $\left(\Phi_i^{n+1} - \Phi_i^n\right)$ will be zero for steady-state flow problems, and will have specified values for unsteady flow problems.

The implicit boundary conditions outlined above represent approximate, quasi-two-dimensional, nonreflecting boundary conditions which can be used for steady and unsteady flow simulations.

Explicit Inlet B.C.'s

For steady flows, the two-dimensional, nonreflecting boundary condition theory of Giles [25,35] can be used. According to this theory, the changes in the characteristic variables at each point on the inlet boundary are comprised of an average change along the boundary and a local change due to harmonic variations in the characteristic variables.

The average changes are determined through the specification of the entropy, flow angle (or tangential velocity), and the stagnation enthalpy. Thus,

$$R_1 = \delta s = \bar{s} - s_{-\infty} \tag{2.23}$$

$$R_2 = (\rho a)\delta v = (\rho a)\left(\bar{v} - \bar{u}\ tan\beta_{-\infty}\right) \tag{2.24}$$

$$R_3 = \rho\delta H_t = \rho\left(\bar{H}_t - H_{t_{-\infty}}\right) \tag{2.25}$$

where $s = P/\rho^\gamma$ is the nonlinear entropy, β is the inlet flow angle, H_t is the stagnation enthalpy, and a is the speed of sound. The overbars denote average values.

The update to the average changes are determined using one step of a Newton-Raphson procedure

$$\begin{bmatrix} \delta R_1 \\ \delta R_2 \\ \delta R_3 \end{bmatrix}^n + \frac{\partial(\delta R_1, \delta R_2, \delta R_3)}{\partial(w_1, w_2, w_3)} \begin{bmatrix} \delta\bar{w}_1 \\ \delta\bar{w}_2 \\ \delta\bar{w}_3 \end{bmatrix} = 0 \tag{2.26}$$

where w_1, w_2, w_3, and w_4 are the characteristic variables

$$w_1 = -\rho a^2 + P \tag{2.27}$$

$$w_2 = \rho a v \tag{2.28}$$

$$w_3 = \rho a u + P \tag{2.29}$$

$$w_4 = -\rho a u + P \tag{2.30}$$

By inverting Eqn. 2.26, one can obtain the average changes to w_1, w_2, and w_3. The local contributions to the total changes, which are due to changes in the characteristic variables

along the boundary, are calculated with the aid of discrete Fourier transforms [35]. The discrete Fourier transform of the outgoing characteristic, w_4, is calculated as

$$w_{4k} = \frac{1}{N}\sum_{j=1}^{N} w_{4j} exp\left(\frac{-i2\pi jk}{N}\right) \tag{2.31}$$

where N is the number of grid points along the inlet boundary. According to Giles [35], the Fourier transform of the second characteristic is

$$w_{2ks} = -\frac{\alpha + M_y}{1 + M_x} w_{4k} \tag{2.32}$$

$$\alpha = i\ sign(k)\sqrt{1 - M^2} \tag{2.33}$$

The correct steady-state change in the second characteristic can then be transformed back to the physical domain as

$$w_{2js} = \sum_{k=-N/2+1}^{N/2-1} w_{2ks} exp\left(\frac{i2\pi jk}{N}\right) \tag{2.34}$$

The ideal correction to the second characteristic variable is then the difference between the correct change and the current value.

$$\delta w_{2js} = \bar{w}_{2js} - w_{2j} \tag{2.35}$$

The conditions that the local entropy and stagnation enthalpy should be equal to their average values are used to determine the steady-state corrections to the first and third characteristic variables [35].

$$\delta R_{1j} = s_j - \bar{s} \tag{2.36}$$

$$\delta R_{3j} = \rho\left(H_{t_j} - \bar{H}_t\right) \tag{2.37}$$

Setting up a Newton-Raphson equation similar to Eqn. 2.26 and solving yields

$$\delta w_{1js} = -R_{1j} \tag{2.38}$$

$$\delta w_{3js} = -\frac{2\left(\frac{1}{\gamma-1}\delta w_{1js} + M_y \delta w_{2js} + R_{3j}\right)}{1 + M_x} \tag{2.39}$$

The total changes in the characteristic variables are then equal to the local changes plus the average changes.

$$\delta w_{1j} = \sigma\left(\delta \bar{w}_1 + \delta w_{1js}\right) \tag{2.40}$$

$$\delta w_{2j} = \sigma\left(\delta \bar{w}_2 + \delta w_{2js}\right) \tag{2.41}$$

$$\delta w_{3j} = \sigma\left(\delta \bar{w}_3 + \delta w_{3js}\right) \tag{2.42}$$

In the above equations, σ is an under-relaxation parameter used to assure the formulation is well-posed [35]. Setting $\sigma = 1/N$ works well for most applications.

The fourth characteristic variable, w_4, is calculated using the interior flow algorithm, or by linear extrapolation. Thus, having calculated the changes in the four characteristic variables, the inlet values of the conservative flow variables can be updated.

For unsteady flows, fully two-dimensional explicit boundary conditions can also be formulated based upon the work of Giles [35]. In this method, the characteristic variables are written in perturbation form such that

$$\begin{bmatrix} w'_1 \\ w'_2 \\ w'_3 \\ w'_4 \end{bmatrix} = \begin{bmatrix} -a^2 & 0 & 0 & 1 \\ 0 & 0 & \rho a & 0 \\ 0 & \rho a & 0 & 1 \\ 0 & -\rho a & 0 & 1 \end{bmatrix}_{\mp\infty} \begin{bmatrix} \delta\rho \\ \delta u \\ \delta v \\ \delta P \end{bmatrix} \tag{2.43}$$

and

$$\begin{bmatrix} \delta\rho \\ \delta u \\ \delta v \\ \delta P \end{bmatrix} = \frac{1}{2} \begin{bmatrix} -2M & 0 & M & M \\ 0 & 0 & N & -N \\ 0 & 2N & 0 & 0 \\ 0 & 0 & 1 & 1 \end{bmatrix}_{\mp\infty} \begin{bmatrix} w'_1 \\ w'_2 \\ w'_3 \\ w'_4 \end{bmatrix} \tag{2.44}$$

where $M = 1/a^2$, $N = 1/(\rho a)$, $\delta\rho = \rho - \rho_{inlet/exit}$, $\delta u = u - u_{inlet/exit}$, $\delta v = v - v_{inlet/exit}$, and $\delta P = P - P_{inlet/exit}$. The subscripts '$-\infty$' and '$+\infty$' refer to the underlying steady flow variables at the inlet and the exit, respectively, and the subscripts '*inlet*' and '*exit*' refer to the prescribed unsteady flow variables at the inlet and the exit boundary. The two-dimensional boundary condition update calculates the changes in the incoming characteristic waves based on the values of the outgoing characteristic waves [25,35]. Since the outgoing characteristic waves are determined from the governing equations in the implicit portion of the numerical procedure, these explicit boundary conditions are easily incorporated into the framework of an implicit analysis. According to Giles [35], the incoming characteristics are determined by

$$\frac{\partial}{\partial t} \begin{bmatrix} w'_1 \\ w'_2 \\ w'_3 \end{bmatrix} + \begin{bmatrix} v & 0 & 0 & 0 \\ 0 & v & R & Q \\ 0 & Q & v & 0 \end{bmatrix}_{-\infty} \frac{\partial}{\partial y} \begin{bmatrix} w'_1 \\ w'_2 \\ w'_3 \\ w'_4 \end{bmatrix} = 0 \tag{2.45}$$

where $Q = (a - u)/2$ and $R = (a + u)/2$. Equation 2.45 can be solved implicitly by inverting a block tridiagonal matrix, where implicit second-difference dissipation is added to the equations to prevent odd-even decoupling.

The prescribed unsteady flow variables at the inlet and exit boundaries can be determined analytically [29,30], be based on experimental data, or be based on a previous numerical solution. In the current investigation, the prescribed flow variables at the inlet/exit of a given blade row are determined using the conditions from numerical simulations for the adjacent upstream/downstream blade rows.

For characteristic waves leaving the computational domain at an angle θ to the boundary, the explicit two-dimensional boundary conditions described above will produce an artificially reflected wave of amplitude $\mathcal{O}(\theta^2)$, compared to $\mathcal{O}(\theta)$ for the quasi-two-dimensional boundary conditions [35].

2.3.2 Exit Boundary Conditions

If the flow leaving the computational domain is subsonic, then three eigenvalues are positive, and one eigenvalue is negative. This means that three characteristic waves (the entropy wave, one pressure wave, and the vorticity wave) are leaving the computational domain and are calculated using the interior flow algorithm, while the fourth characteristic wave (the second pressure wave) is entering the computational domain from downstream and must be specified. At the computational exit, the average static pressure or the upstream travelling Reimann invariant can be specified to represent the upstream-propagating pressure wave. Ideally, the upstream travelling Reimann invariant (which represents the proper quasi-two-dimensional nonreflecting boundary condition) should be specified instead of the average static pressure (which can be reflective on truncated computational domains). For unsteady flow simulations, which are calculated as perturbations to a steady flow solution, it is indeed convenient to specify the upstream travelling Reimann invariant. For steady flow simulations, however, the information needed to accurately specify the Reimann invariant (velocity and speed of sound) is not always known, necessitating the use of the average static pressure as the exit boundary condition.

Implicit Exit B.C.'s

The implicit exit boundary conditions are solved in a manner similar to the implicit boundary conditions used at the inlet boundary. The equations of motion are premultiplied by the matrix of left eigenvectors and the exit selection matrix, L_e, which is written as

$$L_e = \begin{bmatrix} 1 & 0 & 0 & 0 \\ 0 & 1 & 0 & 0 \\ 0 & 0 & 1 & 0 \\ 0 & 0 & 0 & 0 \end{bmatrix} \tag{2.46}$$

The vector containing the exit boundary variables, Φ_e, is given by

$$\Phi_e = \begin{bmatrix} 0 \\ 0 \\ 0 \\ \bar{P} \quad (R^-) \end{bmatrix} \tag{2.47}$$

As before, the implicit boundary conditions described above represent approximate, quasi-two-dimensional, nonreflecting boundary conditions.

Explicit Exit B.C.'s

The development of the steady, explicit, exit boundary conditions are again based on the work of Giles [25,35]. The outline of the theory is similar to that explained above for the explicit inlet boundary conditions.

The average change in the upstream-moving characteristic is based on the specification of an average exit pressure

$$\delta\bar{w}_4 = -2\left(\bar{P} - P_{exit}\right) \tag{2.48}$$

where P_{exit} is the specified exit pressure. The local changes in the upstream-propagating characteristic are calculated as a function of the downstream-moving characteristics. Thus, the discrete Fourier transforms of the vorticity and downstream-propagating pressure waves are calculated.

$$w_{2k} = \frac{1}{N}\sum_{j=1}^{N} w_{2j} exp\left(\frac{-i2\pi jk}{N}\right) \tag{2.49}$$

$$w_{3k} = \frac{1}{N}\sum_{j=1}^{N} w_{3j} exp\left(\frac{-i2\pi jk}{N}\right) \tag{2.50}$$

According to Giles [35] the correct value of the upstream-propagating characteristic variable is given by

$$w_{4ks} = \frac{2M_x}{\alpha - M_y} w_{2k} - \frac{\alpha + M_y}{\alpha - M_y} w_{3k} \tag{2.51}$$

Upon transforming back to the physical domain, this becomes

$$w_{4js} = \sum_{k=-N/2+1}^{N/2-1} w_{4ks} exp\left(\frac{i2\pi jk}{N}\right) \tag{2.52}$$

The ideal local change is given by

$$\delta w_{4js} = w_{4js} - w_{4j\_\_} \tag{2.53}$$

and the total change in the steady upstream-propagating characteristic is given by

$$\delta w_{4j} = \sigma\left(\delta \bar{w}_4 + \delta w_{4js}\right) \tag{2.54}$$

Similar to the explicit unsteady inlet boundary condition procedure, fully two-dimensional, unsteady exit boundary conditions can be implemented into the numerical analysis. The incoming characteristic at the exit boundary is determined by

$$\frac{\partial w'_4}{\partial t} + \begin{bmatrix} 0 & u_{+\infty} & 0 & v_{+\infty} \end{bmatrix} \frac{\partial}{\partial y} \begin{bmatrix} w'_1 \\ w'_2 \\ w'_3 \\ w'_4 \end{bmatrix} = 0 \tag{2.55}$$

Equation 2.55 is solved for w'_4 along the exit boundary by inverting a scalar tridiagonal matrix, where implicit second difference dissipation is added to the equation to prevent odd-even decoupling. As at the inlet, for waves leaving the computational domain at an angle θ to the boundary, the explicit two-dimensional boundary conditions will produce an artificially reflected wave of amplitude $\mathcal{O}(\theta^2)$, compared to $\mathcal{O}(\theta)$ for the quasi-two-dimensional boundary conditions [25,35].

More details on the inlet, exit, and surface boundary conditions can be found in Ref. 30.

2.3.3 Periodic Boundary Conditions

The periodic boundary conditions in the numerical analysis are solved implicitly by using the metric information and dependent flow variables from the grid corresponding to other side of the boundary. The implicit solution technique for the periodic boundary conditions is necessary to obtain time-accurate solutions.

2.3.4 Zonal Boundary Conditions

In the two- and three-dimensional procedures, the use of overlaid grids requires the application of zonal boundary conditions. Dirichlet conditions, in which the time rate change in the conserved variable vector, Q, is set to zero, are imposed at the overlaid boundaries of the O- and H-type grids. The flow variables of Q at these zonal boundaries are explicitly updated after each time step by interpolating values from the adjacent grid. Because of the explicit application of the zonal boundary conditions, large time steps necessitate the use of more than one Newton iteration to maintain time accuracy. The accuracy of information transfer between adjacent grids can also be enhanced by increasing the amount of overlap region between the O- and H-type grids. The zonal boundary conditions are non-conservative, but the current implementation of the zonal boundary conditions has been shown to yield satisfactory results for transonic and supersonic flows [36]. Further information describing the zonal boundary conditions can be found in Ref. 37.

3. Numerical Results

The geometry considered during this effort has been studied in previous investigations (e.g., Refs. 38–30) and corresponds to a thick, highly-cambered model Exit Guide Vane (EGV) cascade. It is constructed by superimposing the thickness distribution of a NACA four-digit series airfoil, i.e.,

$$T(x) = H_T[2.969x^{1/2} - 1.260x - 3.516x^2 + 2.843x^3 - 1.015x^4], \quad 0 \le x \le 1 \ , \tag{3.1}$$

on a thirteen percent circular-arc camberline. The camber distribution is given by

$$C(x) = H_C - R + [R^2 - (x - 0.5)^2]^{1/2} \ , \quad 0 \le x \le 1 \ , \tag{3.2}$$

where $H_C > 0$ is the height of the circular-arc camber line at midchord and $R = (2H_C)^{-1}(0.25 + H_C^2)$ is the radius of the camber line. The surface coordinates of the blade are therefore given by

$$(X, Y)_B^{\pm} = [x \mp 0.5T(x)\sin\theta \ , \ C(x) \pm 0.5T(x)\cos\theta] \ , \quad 0 \le x \le 1 \ , \tag{3.3}$$

where $\theta = \tan^{-1}(dC/dx)$, and the superscripts + and − refer to the upper and lower surfaces of the blade. The wedge-shaped trailing edge of the original NACA thickness distribution is replaced by a round trailing edge which is assumed to be simultaneously tangent to the original trailing-edge location (at $x = 1$) and the upper and lower surfaces of the airfoil, thereby producing a unique trailing-edge circle. The EGV blade is defined using Eqs. (3.1)–(3.3), where the values of the parameters are: $H_T = 0.12$, $H_C = 0.13$. The geometry is illustrated in Figs. 1 and 2. The blade stagger is 15 degrees and the gap-chord ratio, G, is 0.60. The upstream steady flow angle is $\alpha_1 = 55$ degrees measured counter-clockwise from the axial direction. This corresponds to a moderate incidence angle of approximately 5 degrees. This incidence angle is chosen in order to generate a small-scale leading-edge separation in the undisturbed solution.

Suction-surface transition is specified at $s/s_{t.e.} \approx 0.20$, where s is the arc-length distance measured along the blade surface from the leading-edge point, which is defined as the location of minimum x on the blade surface; $s_{t.e.}$ is the trailing-edge arc length measured along the suction surface. The quantity x is the distance aft of the leading edge measured along the machine axis. Transition on the pressure surface is assumed to occur just aft of the leading-edge stagnation point, in order to eliminate any possibility of pressure-surface cove separation, which might induce additional unsteadiness within the flow field. The free-stream turbulence level, which mildly influences the boundary layer through the low Reynolds number correction in the turbulence model, is assumed to be 10 percent. This large value is chosen in an attempt to suppress the suction-surface trailing-edge separation that is predicted to arise at the incidence angle at which the stator is operating, so that both the perturbation to the base undisturbed flow produced by the aft separation and any unsteadiness that might be associated with the separation is minimized.

The wake disturbance introduced in the wake-stator interaction calculations is modeled by introducing a wake-like profile at the upstream boundary of the mesh. The wake deficit at the upstream boundary is defined by a hyperbolic secant function. The width of the wake is 10% of the blade circumferential spacing, where the width is defined as the distance

between points in the profile at which the value of the function is 10% of its maximum value. The deficit is applied only to the axial component of velocity in the frame of reference of the rotor, and is then transformed to the stator frame of reference by adding to the deficit profile the circumferential velocity component representing the rotation of the upstream rotor. Variations in the other physical quantities (e.g., pressure, density, etc.) at the upstream boundary are obtained as part of the solution using the characteristic conditions at the upstream boundary described in the previous section.

The Reynolds number, Re, for the present calculations is chosen such that the assumption of laminar flow in the neighborhood of the suction-surface leading edge is a reasonable one, based on the local value of the Reynolds number scaled by the leading-edge radius. The Reynolds number based on chord for the calculations carried out here is 300,000; based on leading-edge radius the value is $Re = 4740$. Because of the locally adverse pressure gradient and the associated suction-surface separation bubble, it is realistic to allow for transition within or just aft of the separation bubble. In the present case suction-surface transition is imposed at a fixed surface location a small distance upstream of the time-averaged reattachment location predicted for the case without the rotor wake disturbance. This aspect of the present investigation needs to be examined in greater detail in the future to determine how it influences the conclusions that have been obtained.

The analysis will first be applied in an effort to obtain solutions in the absence of the upstream wakes. After the baseline undisturbed solution has been obtained, the same configuration will be subjected to unsteady wakes convected downstream from the upstream boundary and the interaction of the wake with the suction-surface boundary layer will be examined in detail. All of the calculations were carried out for many periods ($\mathcal{O}(15-30)$) in the case where the wake disturbance is present, and for many characteristic times ($t_C = C/U_\infty$, where C is blade chord and U_∞ is the velocity magnitude far upstream of the cascade) in the case for which the wake disturbance is absent.

It is important to note that the present mesh, while using many more grid points in the inner O-mesh region (551 points around the blade, 81 points normal to the blade; see Figs. 1a-c) than is typically employed for similar calculations, it still falls far short of being able to resolve all of the pertinent features of the flows considered herein. In particular, in deciding to focus on the suction-surface leading-edge region grid, resolution was sacrificed elsewhere on the blade surface. This is particularly noticeable in the neighborhood of the trailing edge and on the pressure surface of the blade.

Two different wake deficits are considered: 5% and 30%. The former represents a very weak wake and would correspond to an unrealistically large rotor-stator axial spacing for modern gas-turbine compressors. However, it serves to illustrate the sensitivity of the separation region to disturbances, and provides a baseline against which the stronger deficit case can be judged. The latter wake deficit corresponds to a rotor-stator spacing of approximately 0.5 chords [3].

3.1 Flow in the Absence of Rotor Wakes

The undisturbed flow solution was obtained on a mesh that is highly refined in the vicinity of the undisturbed flow, suction-surface separation bubble; see Figs. 1a-c. At the blade surface the minimum streamwise mesh spacing is $\Delta s/s_{t.e.} \approx 0.0004$ and the normal

mesh spacing at the first point away from the wall, which is maintained at a constant value everywhere along the airfoil surface, is $\Delta n/C \approx 5 \times 10^{-6}$, where C is the blade chord. This produces a mesh for which the average y^+ at the first point away from the surface over the entire turbulent region is $\mathcal{O}(0.1)$, and places on the order of 20-50 points within the laminar boundary layer, depending on the streamwise location. The temporal stepsize used for the undisturbed flow calculations is the same as that used for the wake-stator interaction calculations described below.

The time-averaged streakline pattern is shown in Figs. 2a-c. A trailing-edge separation bubble spanning approximately 20 percent of blade chord is present. These calculations were carried out with a relatively coarse mesh at the trailing edge. This appears to result in local numerical viscosity of sufficient magnitude to suppress any trailing-edge shedding that might otherwise occur, producing a steady trailing-edge separation. If a finer mesh was used in the vicinity of the trailing edge, unsteady vortex shedding and a possible unsteady interaction between the shedding and the trailing-edge separation bubble would be expected to occur, and to produce relatively mild unsteady loading fluctuations, as demonstrated in Ref. 3, for example. The suppression of the trailing-edge vortex shedding is expected to be of negligible consequence to the local flow structure in the neighborhood of the leading-edge separation, which is the focus of this investigation.

A thin leading-edge separation bubble is present in the solution, as can be seen more clearly in Figs. 2b and c, where the time-averaged separation and reattachment points are denoted by S and R, respectively, and the fixed transition-point location is denoted by T.

The flow in the neigborhood of the leading-edge separation bubble is not steady. Figures 3a-d show the time histories of the surface pressure P and skin-friction coefficient C_f at four points on the blade suction surface, corresponding to locations that are: (1) slightly aft of the time-averaged separation point, (2) just downstream of the specified transition onset location and upstream of the time-averaged reattachment point location, (3) approximately midway between the transition location and the time-averaged reattachment point, and (4) just downstream of the time-average reattachment location. The plot scales were selected to facilitate comparison between the magnitude of the unsteady fluctuations amongst these locations and for later comparison with the results obtained with the wake disturbance included.

The degree of unsteadiness is significantly larger at the two downstream points (3 and 4) than at the upstream points (1 and 2). We believe that this is due to unsteady shedding of vortices from the rear of the separation bubble, evidence of which can be seen in Fig. 4, which shows the instantaneous streaklines in the vicinity of the leading-edge separation bubble associated with the *disturbance* velocity field. The disturbance velocity field is obtained by subtracting the time-averaged components of the velocity field from the instantaneous values of the velocity components at one instant in time. The resulting disturbance field makes it easier to identify features introduced by unsteadiness in the flow, although the interpretation must be made carefully. In the "snapshot" shown in Fig. 4 there is a series of distinct vortices convecting downstream from the bubble. They appear to grow after shortly after forming and after moving downstream some distance they appear to decay. The decay is most likely an artifact of the increased numerical dissipation that is encountered downstream of the bubble where the streamwise grid spacing increases (see Fig. 1). In addition, an unsteady disturbance is evident within and around the region of the bubble, centered in the middle of

the semicircular pattern of streaklines to the left of the center of the plot. This disturbance is believed by the authors to be a product of pulsations of the bubble as vortices are produced and ejected from within it. Further study of the details of the unsteady flow structure is needed to determine whether or not this conjecture is correct.

3.2 Flow in the Presence of Rotor Wakes

The undisturbed solution discussed above was used as the baseline for two sets of calculations performed in the presence of simulated rotor wakes, where the two cases differed in the specified magnitude of the wake velocity deficit. In particular, deficits of 5 and 30 percent of the local (inlet plane) axial velocity were considered. The reduced temporal frequency of the disturbance was the same for both cases. The reduced temporal frequency of the incident wakes is given by

$$\omega = -\frac{\sigma U_{wheel}}{G} , \tag{3.4}$$

where $\sigma = -2\pi$, $U_{wheel} = 1.20$ and $G = 0.60$ producing a reduced frequency of $\omega = 12.57$.

Results for 5 percent wake deficit

The wake can be easily visualized by considering the disturbance flow resulting from its imposition on the baseline flow. The disturbance velocity field in the region between the inflow boundary and the cascade leading edge at one instant of time is shown in Fig. 5. Note that the disturbance to the baseline flow appears as a stream of fluid moving from the suction surface towards the pressure surface.

The effect of the wakes on the blade surface pressure and surface shear stress coefficient are shown in Figs. 6a and b, where time histories are presented at four different stations on the suction surface over a time span of $2.5T$, where $T = 1.0$ in the nondimensional time variable, τ. The effect of the passing wake is evident at all four stations. At the three most forward stations a small rise in pressure and a concommitant decrease in the shear stress occurs as the wakes pass those stations. At the farthest aft station the nature of the unsteadiness is quite different from that observed at the other three stations, with the former having much more frequency content than the latter. The difference is believed to be due to the passage of vortices shed upstream by the separated boundary layer, as will be shown more clearly later. Comparing the results presented in Fig. 6 with those of Fig. 3 shows that the amplitude of the pressure and skin-friction oscillations that are associated with the separation region in the undisturbed flow is *reduced* by the passage of the periodic wakes.

The structure and evolution of the wakes in the region upstream of the cascade and within the blade passages is shown in Fig. 7a-f where a series of instantaneous vorticity contours are presented, showing the convection of the wakes during a single period, T. Although this figure shows the results for the 30 percent wake deficit calculation, the 5 percent deficit result looks nearly identical if the correct contour levels are selected, since the flow conditions and disturbance frequency are the same in both cases. The wakes undergo some smearing as they are convected downstream, as evidenced by the slight spreading of the wake contours with increasing axial distance. The wakes are distorted as they convect within the blade passage rotating in the counter-clockwise direction due to the cross-passage velocity gradient (i.e.,

faster moving fluid on the suction surface than on the pressure surface). In addition, there is some apparent distortion of the wakes at the interface between the outer H-mesh and the inner O-mesh, as seen in Fig. 7. An assessment of the magnitude of these and other possible numerically-induced effects on the flow features should be carried out in the future.

A series of instantaneous disturbance streaklines for the 5 percent wake deficit case is shown in Fig. 8a-f. They display periodic behavior in the larger-scale features (comparing Figs. 8a and 8f), although the small-scale features are not periodic. This may be due to not carrying out the numerical solution far enough in time, or it may be a feature of this complex flow. Comparing Fig. 8 with Fig. 4 reveals some important distinctions between the structure of the two flows. In the undisturbed case shown in Fig. 4 the series of downstream vortices appears to initiate some distance downstream of the structure at the center of the semi-circular feature that is observed. In the case where the wake is present (Fig. 8) the vortices appear to emanate from the center of the similar structure, which changes shape dramatically during the cycle. In addition, the vortical structures appear to be larger in the latter case. In both cases the spacing between the vortices increases significantly upon leaving the neighborhood of their apparent origin. How much of this is due to the change in axial grid resolution in that region is unclear, and this needs to be examined in future work.

Results for 30 percent wake deficit

The effect of the wakes on the blade surface pressure and surface shear stress coefficient are shown in Figs. 9a-d, where time histories are presented at a total of seven different stations on the suction surface over a time span of $2.5T$ where, as before, $T = 0.20$ in the nondimensional time variable, τ. The signature of the passing wake is evident at all seven stations. Whereas for the 5 percent wake case the behavior of the histories changed, particularly at the furthest aft station at $s/s_{t.e.} \approx 0.201$, due to the shedding vortices passing that station, the behavior remains very much similar at all seven stations for the 30 percent wake deficit case. It is also notable that the signature of the wakes in the latter case shows the distinct presence of a second harmonic that is nearly negligible in the 5 percent wake deficit results. The source of the second harmonic is made clear by examining the disturbance streamlines for the 30 percent wake deficit.

The structure and evolution of the wakes in the region upstream of the cascade and within the blade passages was shown in Fig. 7a-f for the 30 percent wake deficit case. A series of instantaneous disturbance streaklines for the 30 percent wake deficit case is shown in Fig. 10a-f. A very strong feature of the flow field in this case is the presence of large cell-like structures that are counter-rotating with respect to their immediate neighbors as they convect through the blade passage. The effect of these cells on the separation region is very strong, with the vortex shedding exhibited in the undisturbed and mild wake-deficit case almost completely suppressed.

In Figs. 11a and b the time-averaged surface pressure and shear stress distributions are shown for the undisturbed case, and for the 5 and 30 percent wake deficit cases. The good overall agreement between the three results indicates that nonlinear effects are relatively weak in the two wake-stator interaction calculations, although the 30 percent wake deficit case shows somewhat more pronounced differences with the undisturbed case than does the 5 percent wake. This is consistent with the stronger disturbance associated with the former

case, for which the degree of nonlinearity is expected to be greatest.

4. Conclusions and Recommendations for Future Work

The results obtained during this study indicate that the use of very fine grids captures small-scale unsteady flow structures associated with the wake-stator suction-surface interaction. Even in the absence of rotor wakes the leading-edge separation bubble displays unsteady shedding of vortices. The presence of wakes, even when the wake velocity deficit is small, can significantly alter the unsteady boundary-layer behavior. However, when the velocity deficit becomes stronger, the unsteady boundary-layer undergoes a significant alteration in behavior, with the vortex shedding suppressed relative to the undisturbed or weak wake deficit cases in the present calculations.

The following tasks are recommended as potentially frutiful tasks for follow-on to this effort:

1. Conduct a grid/timestep study to determine the effect of grid and timestep variations on the present solutions;

2. Extend the region of high grid resolution to encompass the entire suction surface, at minimum, to alleviate some of the concerns expressed herein about the effect of increased numerical dissipation downstream of the fine-grid region in the vorticies form in the separation region;

3. Assess the effect of the O-H grid overlap on solutions of rotor-stator interaction problems, and seek ways to lessen those effects;

4. Examine different geometries and a broader range of parameters, e.g., Reynolds number, incidence angle, disturbance frequency and amplitude;

5. Examine the response of the flow to the incoming wakes; this can help with efforts to model unsteady deterministic effects in turbomachinery using analyses such as the average-passage approach of Adamczyk [41–43].

References

1. Hodson, H. P., "Modeling Unsteady Transition and Its Effects on Profile Loss," *ASME J. of Turbomachinery*, Vol. 112, No. 4, pp. 691-701.

2. Kerrebrock, J. L. and Mikolajczak, A. A., "Intra-stator Transport of Rotor Wakes and its Effect on Compressor Performance," ASME Paper 70-GT-39, 1970.

3. Valkov, T. V., "Control of the Unsteady Flow in a Stator Blade Row Interating with Upstream Moving Wakes," MIT Gas Turbine Laboratory Report GTL #215, January 1993.

4. Valkov, T. V. and Tan, C. S., "Control of the Unsteady Flow in a Stator Blade Row Interating with Upstream Moving Wakes," ASME Paper 93-GT-23, 1993.

5. Peridier, V. J., Smith, F. T. and Walker, J. D. A., "Vortex-induced Boundary-layer Separation. Pt. 1, The Limit Problem Re$\rightarrow \infty$," *J. Fluid Mech.*, Vol. 232, Nov. 1991, pp. 99-131.

6. Peridier, V. J., Smith, F. T. and Walker, J. D. A., "Vortex-induced Boundary-layer Separation. Pt. 2, Unsteady Interacting Boundary-layer Theory," *J. Fluid Mech.*, Vol. 232, Nov. 1991, pp. 133-165.

7. Reisenthel, P. H. and Childs, R. E., "A Study of Reynolds Number Effects on Incipient Leading Edge Stall," AIAA Paper 94-2339, 1994.

8. Reisenthel, P. H., "Further Results on the Reynolds Number Scaling of Incipient Leading Edge Stall," AIAA Paper 95-0780, 1995.

9. Bhaskaran, R., and Rothmayer A. P., "A Navier-Stokes Solution for the Leading-Edge Flow Past Pitching and Oscillating Airfoils, in preparation, 1995.

10. Carr, L., "Progress in Analysis and Prediction of Dynamic Stall," *J. Aircraft*, Vol. 25, Jan. 1988, pp. 6-17.

11. Carr, L. and McCroskey, W. J., "A Review of Recent Advances in Computational and Experimental Analysis of Dynamic Stall," International Union of Theoretical and Applied Mechanics Symposium on Fluid Dynamics of High Angle of Attack," Tokyo, Japan, Sept. 1992.

12. Smith, F. T., "Concerning Dynamic Stall," *The Aeronautical Quarterly*, Vol. XXXIII, Part 4, Nov. 1982, pp. 331–352.

13. Smith, F. T., "Finite-time Break-up can Occur in Any Unsteady Interacting Boundary Layer," *Mathematika*, Vol. 35, No. 70, 1988, pp. 256-273.

14. Elliott, J. W. and Smith, F. T., "Dynamic Stall Due to Unsteady Marginal Separation," *J. Fluid Mech.*, Vol. 179, 1987, pp. 489–512.

15. Doligalski, T. L., "CFD Challenges for the U.S. Army," AIAA Paper 93-3295, 1993.

16. Choudhuri, P. Ghosh, Knight, D. D. and Visbal, M. R., "Two-Dimensional Unsteady Leading-Edge Separation on a Pitching Airfoil," *AIAA J.*, Vol. 32, No. 4, April 1994, pp. 673–681.

17. Mehta, U. B. and Zalman, L., "Starting Vortex, Separation Bubbles and Stall: A Numerical Study of Laminar Unsteady Flow Around an Airfoil," *J. Fluid Mech.*, Vol. 67, Pt. 2, 1975, pp. 227–256.

18. Ghia, K.N., Yang, J., Osswald, G.A. and Ghia, U., "Study of the Role of Unsteady Separation in the Formation of Dynamic Stall Vortex," AIAA Paper 92-0196, 1992.

19. Visbal, M. R., "Dynamic Stall of a Constant-Rate Pitching Airfoil, *J. Aircraft*, Vol. 27, No. 5, pp. 400-407.

20. Patterson, M. T. and Lorber, P. F., "Computational and Experimental Studies of Compressible Dynamic Stall," *J. of Fluids and Structures,* Vol. 4, pp. 259-285, 1990.

21. Verdon, J. M., "Unsteady Aerodynamic Methods for Turbomachinery Aeroelastic and Aeroacoustic Applications," *AIAA J.*, Vol. 31, No. 1, Jan. 1993, pp. 235-250, pp. 235-250.

22. Dring, R. P., Joslyn, H. D., Hardin, L. W. and Wagner, J. H., "Turbine Rotor-Stator Interaction," *J. Engrg. for Power*, Vol. 104, No. 4, 1982, pp. 729-742.

23. Hodson, H. P., "An Inviscid Blade-to-Blade Prodiction of Wake-Generated Unsteady Flow," ASME Paper 84-GT-43, 1984.

24. Rai, M. M., "Navier-Stokes Simulations of Rotor/Stator Interaction Using Patched and Overlaid Grids," *AIAA J. of Propulsion and Power*, Vol. 3, No. 5, Sept.-Oct. 1987.

25. Giles, M., "UNSFLO: A Numerical Method for the Calculation of Unsteady Flow in Turbomachinery," GTL Report No. 205, Gas Turbine Laboratory, Massachusetts Institute of Technology, 1991.

26. Baldwin, B. S. and Lomax, H., "Thin-Layer Approximation and Algebraic Model for Separated Turbulent Flows," AIAA Paper 78-257, 1978.

27. Dwahan, S., and Narasimha, R., "Some Properties of Boundary Flow During Transition from Laminar to Turbulent Motion," *Journal of Fluid Mechanics*, Vol. 3, 1958, pp. 418-436.

28. Chakravarthy, S. R. and Osher, S., "Numerical Experiments with the Osher Upwind Scheme for the Euler Equations," AIAA Paper 82-0975, 1982.

29. Dorney, D. J., and Verdon, J. M., "Numerical Simulations of Unsteady Cascade Flows," ASME Paper 93-GT-87, Cincinnati, OH, 1993, also to be published in *ASME Journal of Turbomachinery.*

30. Dorney, D. J., *Numerical Simulations of Unsteady Flows in Turbomachines*, Ph.D. thesis, The Pennsylvania State University, University Park, PA, 1992.

31. Dorney, D. J., Davis, R. L., and Edwards, D. E., "Investigation of Hot Streak Migration and Film Cooling Effects on Heat Transfer in Rotor/Stator Interacting Flows, Final Report," N000140-88-C-0677, April, 1992.

32. Sorenson, R. L., " A Computer Program to Generate Two-Dimensional Grids about Airfoils and Other Shapes by the Use of Poisson's Equation," NASA TM-81198, 1980.

33. Chakravarthy, S. R., "Euler Equations- Implicit Schemes and Implicit Boundary Conditions," AIAA Paper 82-0228, 1982.

34. Rai, M. M. and Chaussee, D. S., " New Implicit Boundary Procedures - Theory and Applications," *AIAA Journal*, pp. 1094-1100, 1984.

35. Giles, M. B., "Nonreflecting Boundary Conditions for Euler Equation Calculations," *AIAA Journal*, Vol.28, No. 12, December, 1990, pp. 2050-2058.

36. Steinke, R. J., "Application of a Two-Dimensional Unsteady Viscous Analysis Code to a Supersonic Throughflow Fan Stage," NASA TM 4141, November, 1989.

37. Rai, M. M., "Navier-Stokes Simulations of Rotor/Stator Interaction Using Patched and Overlaid Grids," *AIAA Journal of Propulsion and Power*, Vol. 3, No. 5, September-October 1987.

38. Verdon, J. M. and Hall, K. C., "Development of a Linearized Unsteady Aerodynamic Analysis for Cascade Gust Response Predictions," NASA CR 4308, July 1990.

39. Verdon, J. M., Barnett, M., Hall, K. C. and Ayer, T. C., "Development of Unsteady Aerodynamic Analyses for Turbomachinery Aeroelastic and Aeroacoustic Applications," NASA CR 4405, October 1991.

40. Barnett, M., Verdon, J. M. and Ayer, T. C., "An Analysis for High Reynolds Number Inviscid/Viscid Interactions in Cascades," NASA CR 4519, May 1993.

41. Adamczyk, J. J., "Model Equation for Simulating Flows in Multistage Turbomachinery," NASA TM-86869, November 1984.

42. Adamczyk, J. J., "A Model for Closing the Inviscid Form of the Average-Passage Equation System," NASA TM-87199, 1986.

43. Adamczyk, J. J., Celestina, M. L., Beach, T. A. and Barnett, M., "Simulation of Three-Dimensional Viscous Flow within a Multistage Turbine, *Transactions of the ASME, Journal of Turbomachinery*," Vol. 112, No. 3, 1990, pp. 370-376.

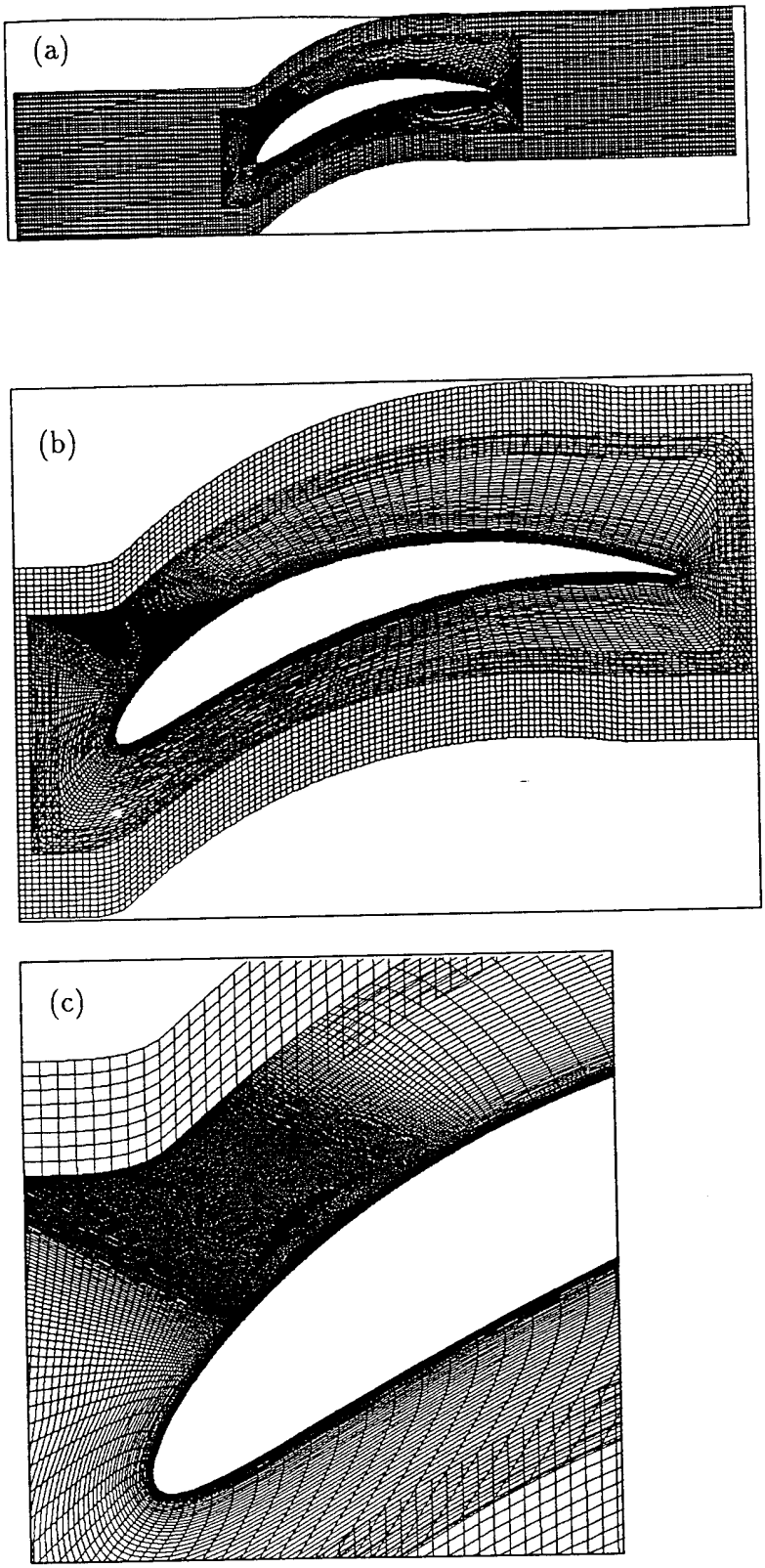

Figure 1: Overlaid O-H grids used for EGV calculations: (a) complete grid system; (b) detail view of O-grid; (c) detail view of fine-grid region.

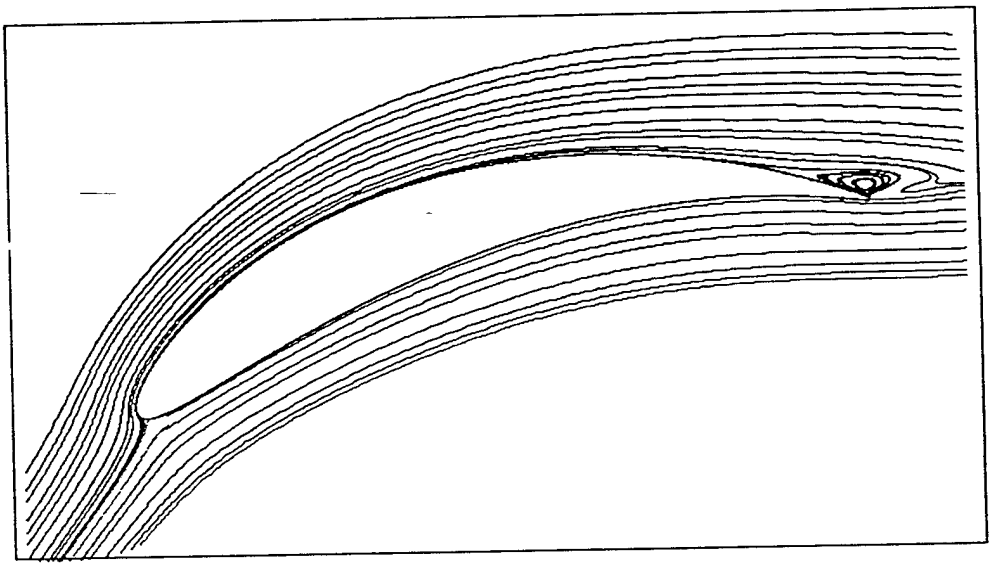

Figure 2: (a) Time-averaged streakline pattern for EGV in absence of wake disturbances: $Re = 300,000$, $\alpha_1 = 55$ deg.

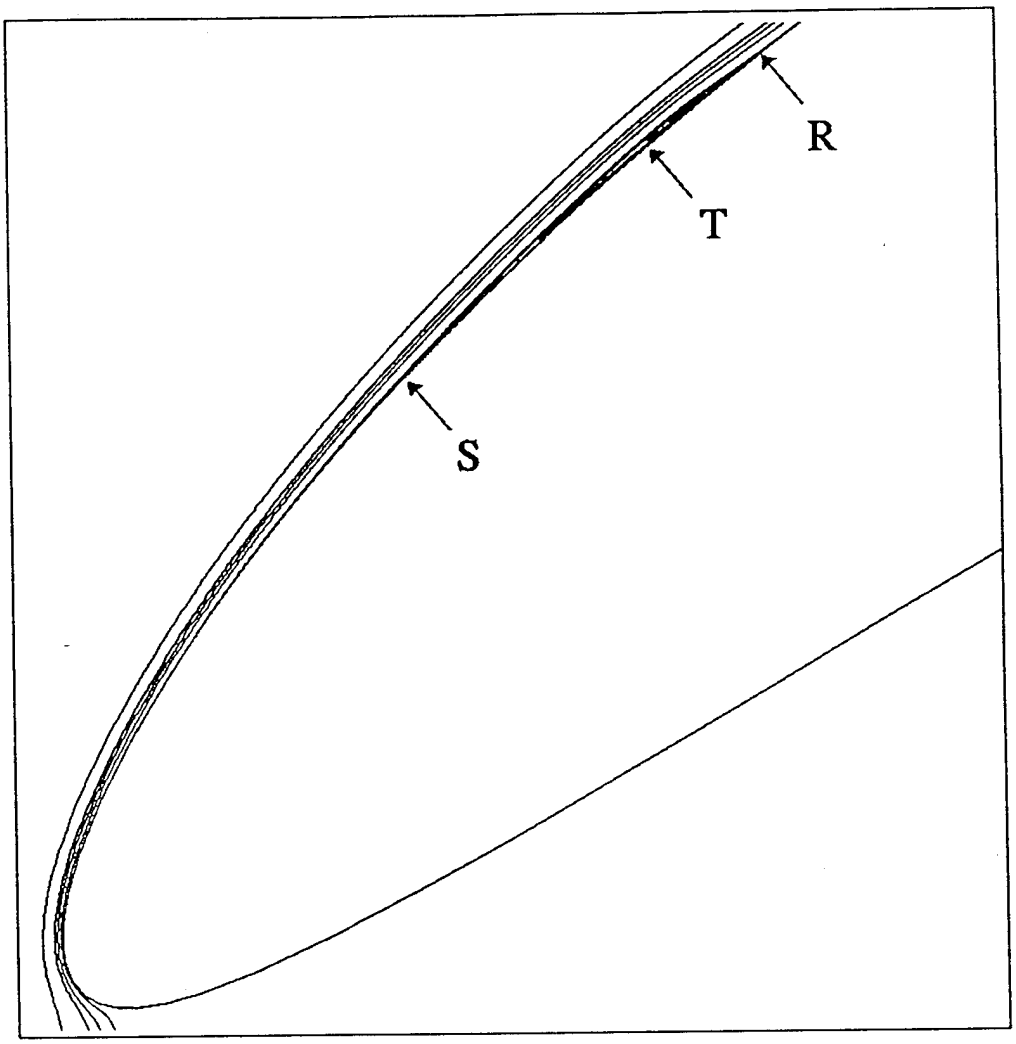

Figure 2: (b) Detail of time-averaged streakline pattern for forward portion of EGV in absence of wake disturbances.

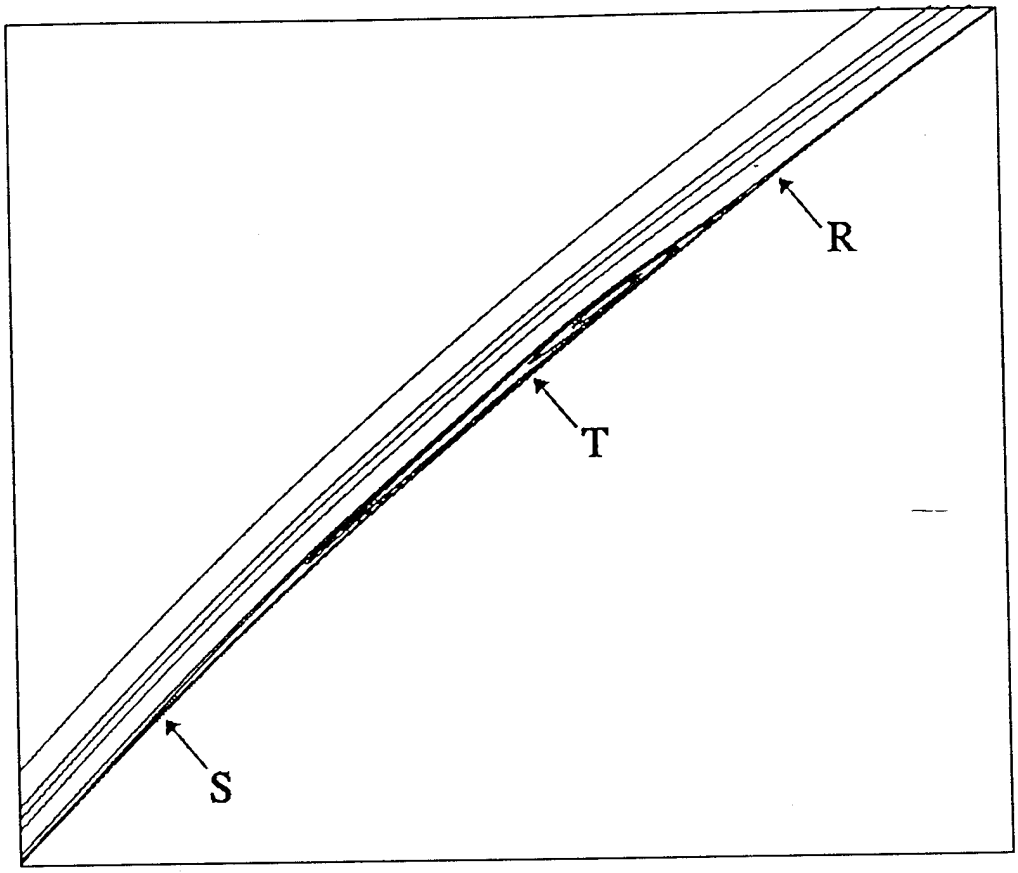

Figure 2: (c) Detail of time-averaged streakline pattern in vicinity of leading-edge separation of EGV in absence of wake disturbances.

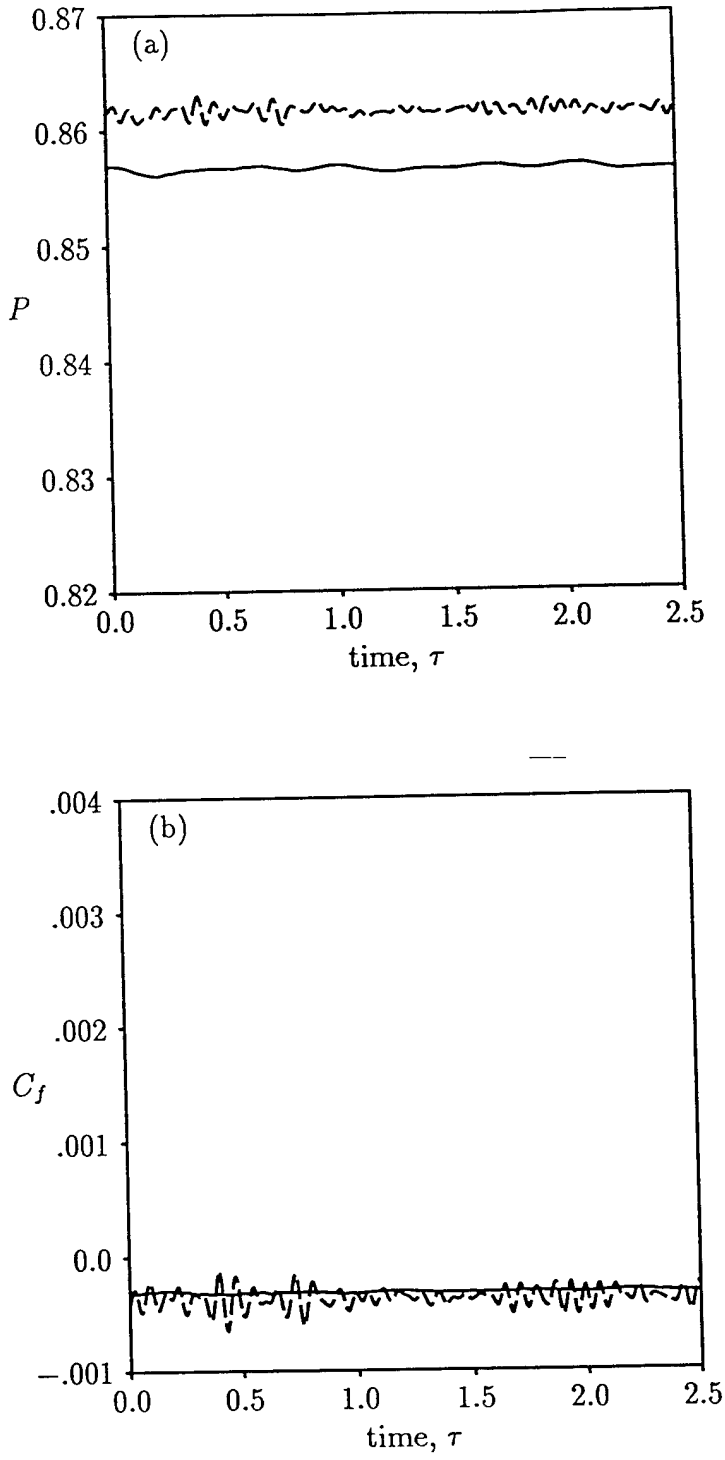

Figure 3: (a) Surface-pressure and (b) surface shear-stress time histories at two axial stations for undisturbed flow in an EGV cascade, $Re = 300,000, M_1 \approx 0.42$: ——: $s/s_{t.e.} \approx 0.163$, $\approx 4\%$ $s/s_{t.e.}$ aft of time-averaged separation point; — — —: $s/s_{t.e.} \approx 0.201$, just downstream of start of transition, upstream of time-averaged reattachment location.

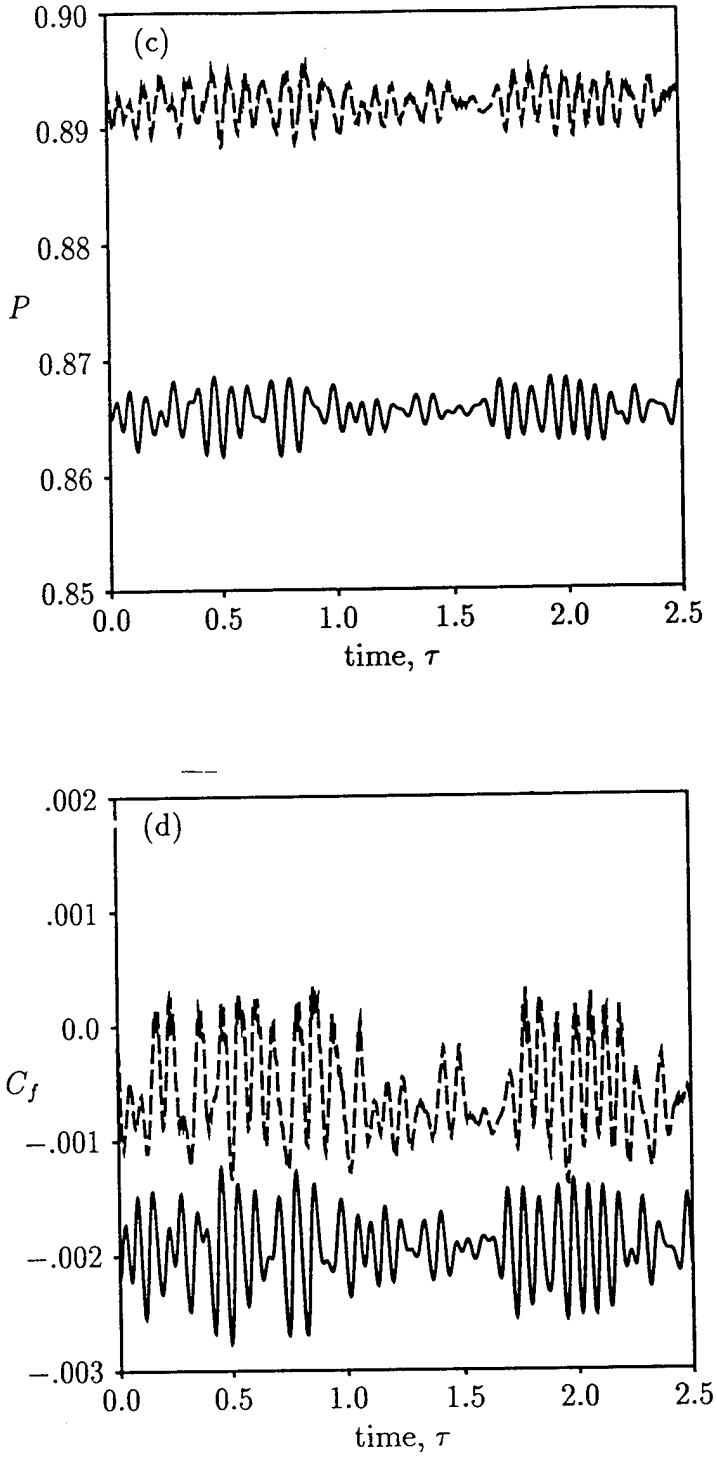

Figure 3: (c) Surface-pressure and (d) surface shear-stress time histories at two axial stations for undisturbed flow in an EGV cascade, $Re = 300,000, M_1 \approx 0.42$: ——: $s/s_{t.e.} \approx 0.217$, between transition and time-averaged reattachment locations; — — —: $s/s_{t.e.} \approx 0.237$, near time-averaged reattachment location.

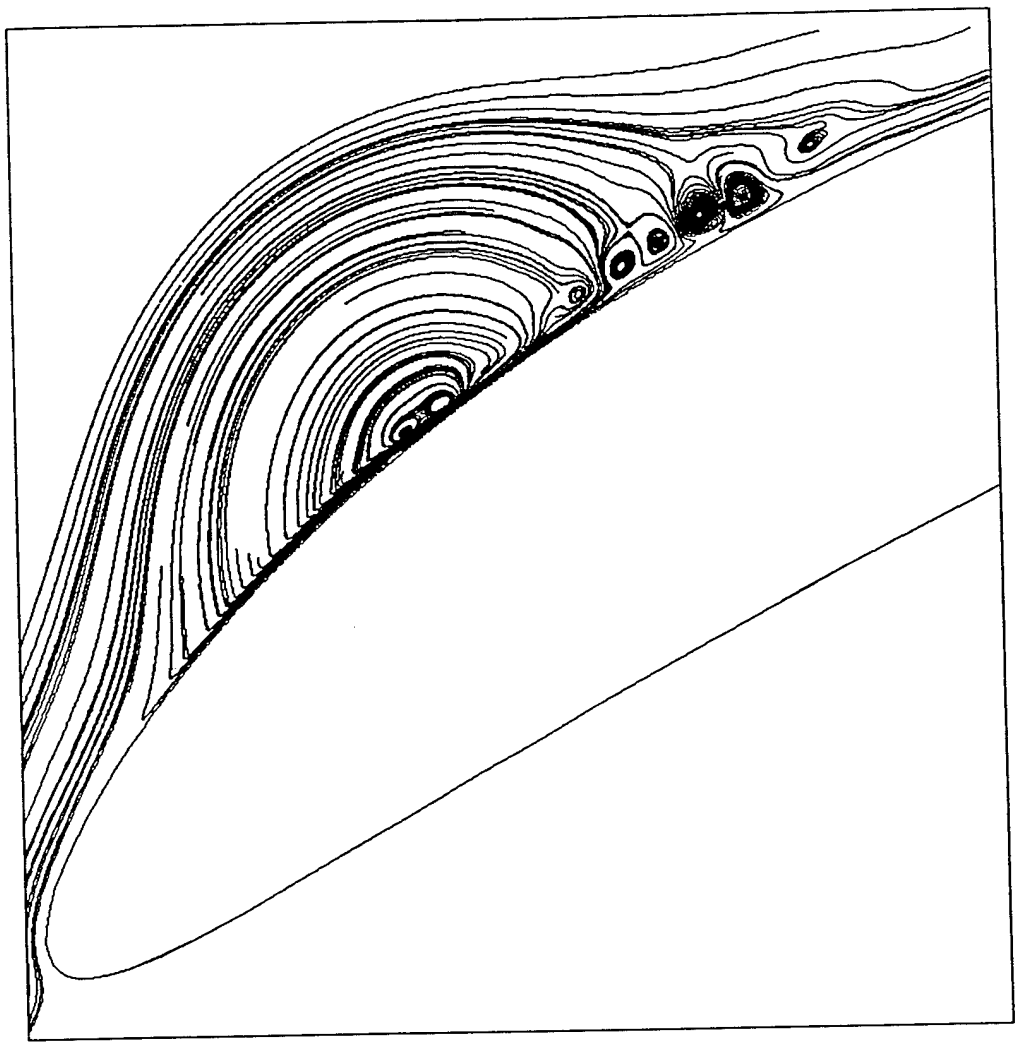

Figure 4: Instantaneous disturbance streakline pattern for EGV in absence of rotor wakes: $Re = 300,000$, $\alpha_1 = 55$ deg.

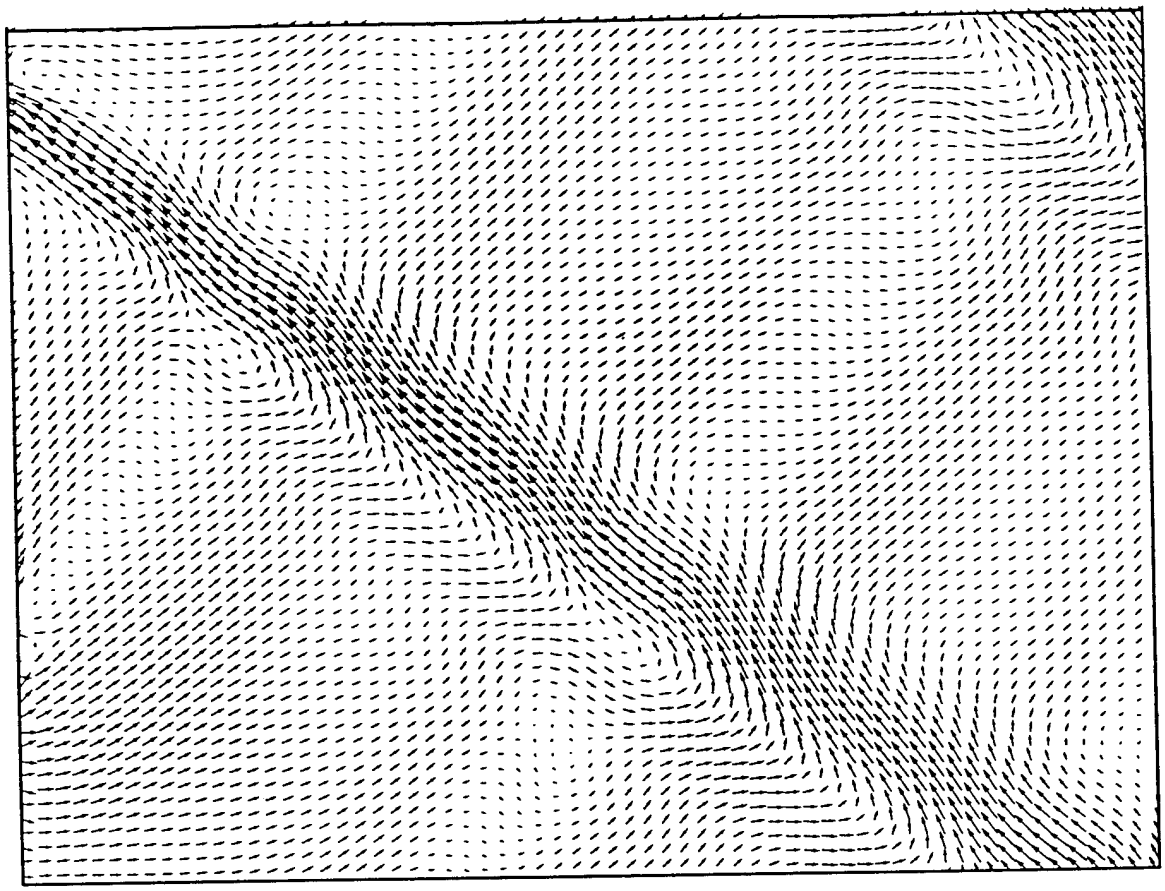

Figure 5: Instantaneous disturbance velocity vectors upstream of EGV cascade for 5 percent wake deficit calculation.

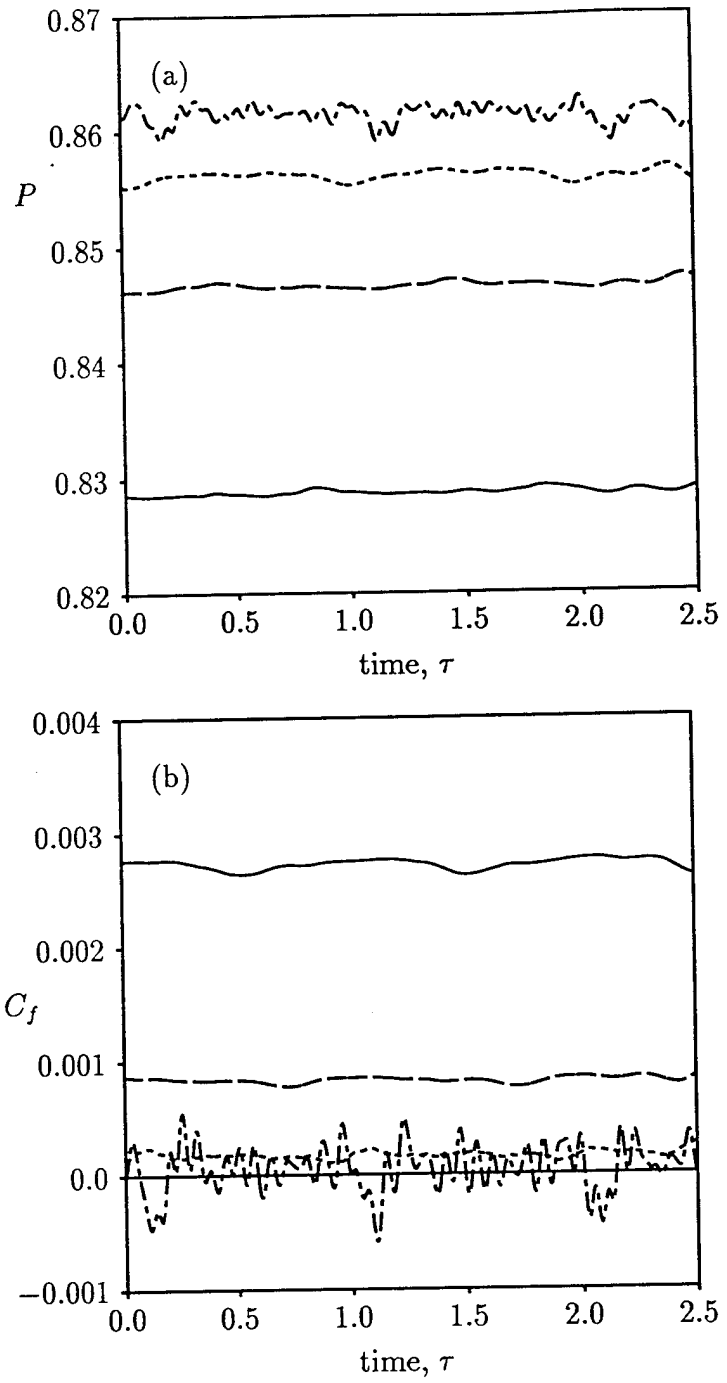

Figure 6: (a) Surface-pressure and (b) surface shear stress time histories at four axial stations for flow in EGV cascade exposed to wakes with 5 percent velocity deficit; $Re = 300,000$, $M_1 \approx 0.42$, $\alpha_1 = 55$ deg: ——: $s/s_{t.e.} \approx 0.100$, upstream of the time-averaged separation location; — — —: $s/s_{t.e.} \approx 0.129$, just upstream of the time-averaged separation location; - - - - - -: $s/s_{t.e.} \approx 0.163$, about midway between the time-averaged separation point and the fixed transition location; — - — - —: $s/s_{t.e.} \approx 0.201$, just downstream of the start of transition, and upstream of the time-averaged reattachment location.

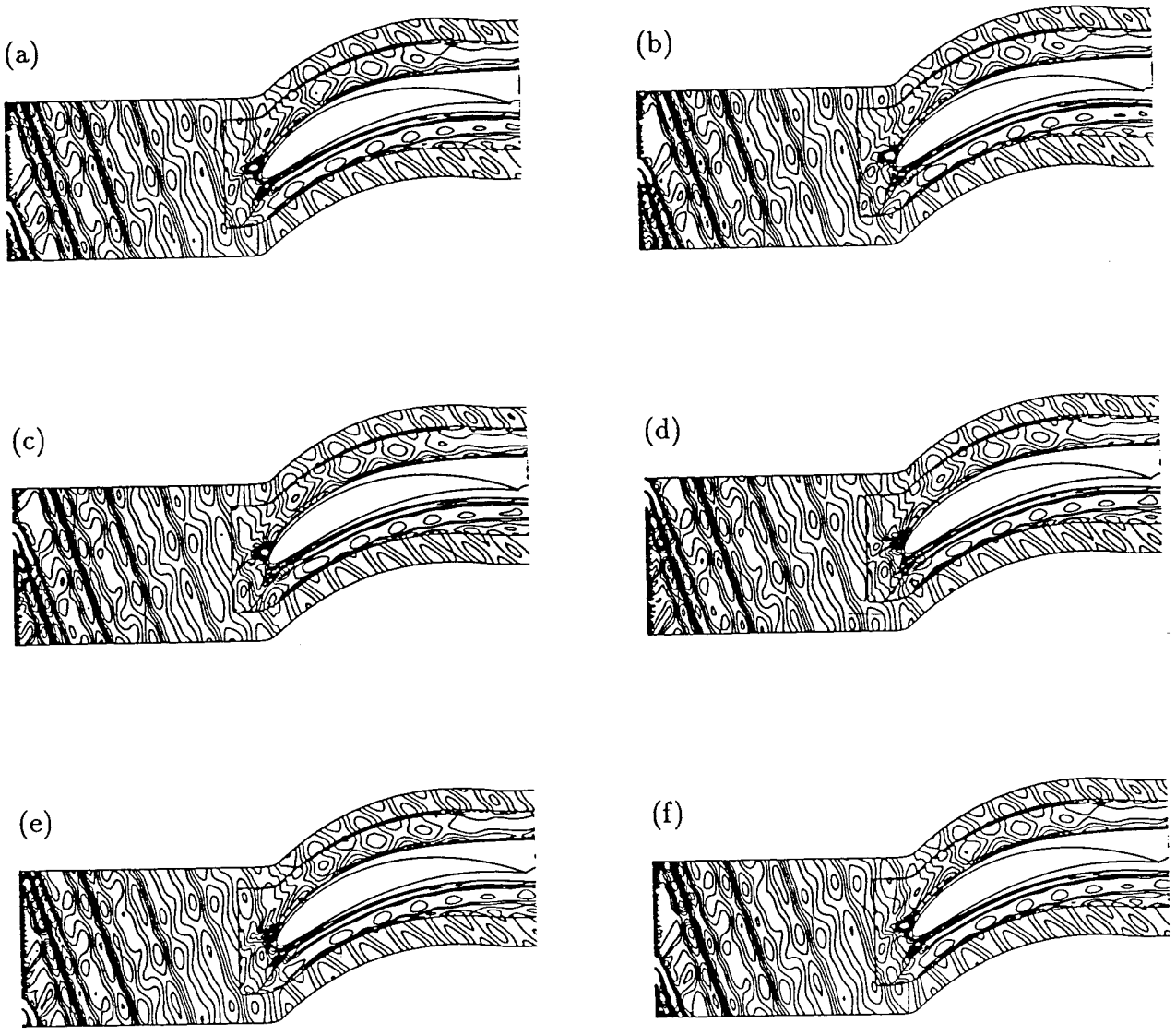

Figure 7: *Disturbance vorticity* for 30% wake deficit EGV calculation; (a) $T + 0T$; (b) $T + 0.2T$; (c) $T + 0.4T$; (d) $T + 0.6T$; (e) $T + 0.8T$; (f) $T + 1.0T$.

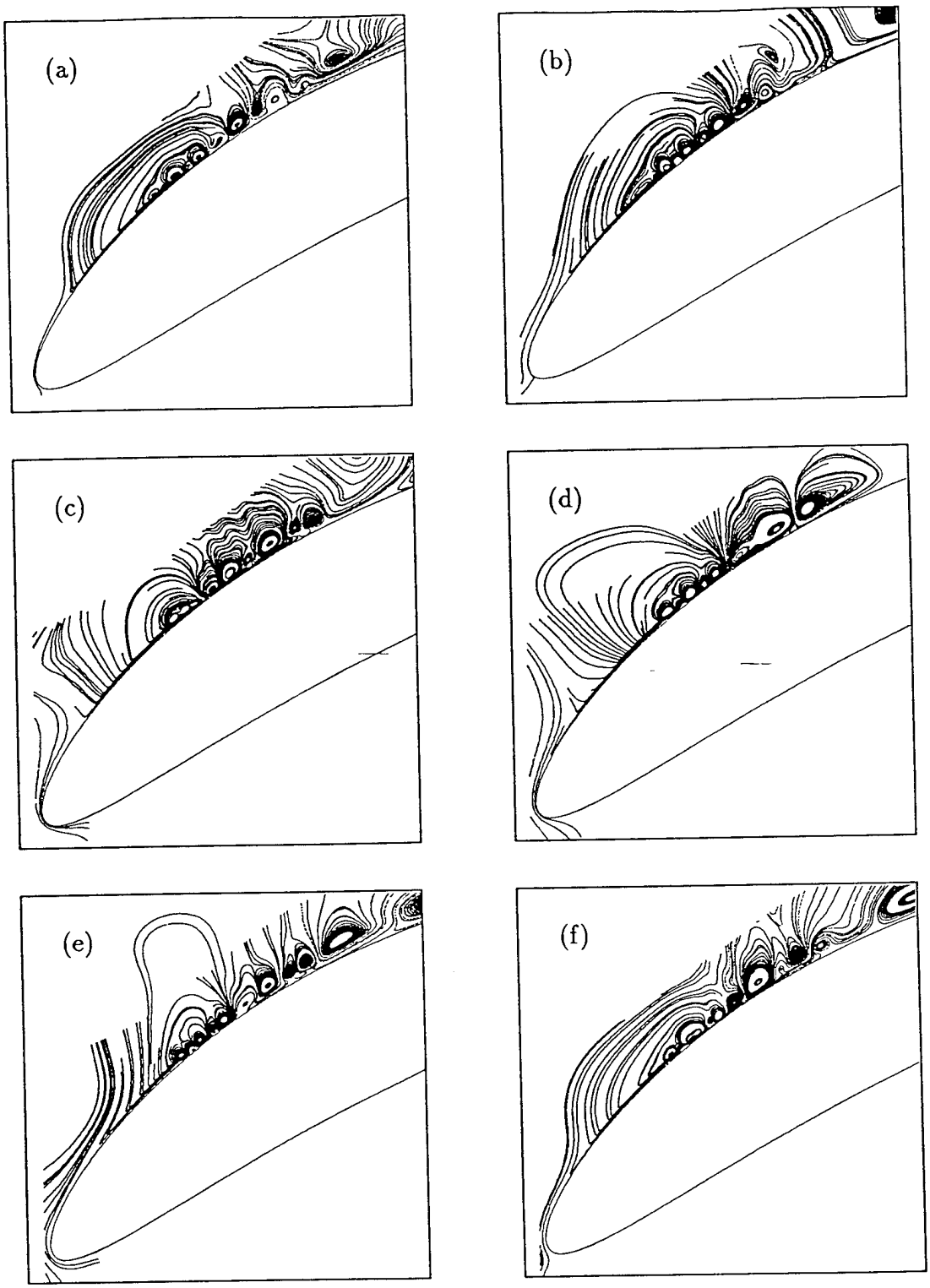

Figure 8: Instantaneous disturbance streakline patterns for EGV in presence of rotor wakes with 5 percent velocity deficit: (a) $T + 0T$; (b) $T + 0.2T$; (b) $T + 0.4T$; (b) $T + 0.6T$; (b) $T + 0.8T$; (b) $T + 1.0T$.

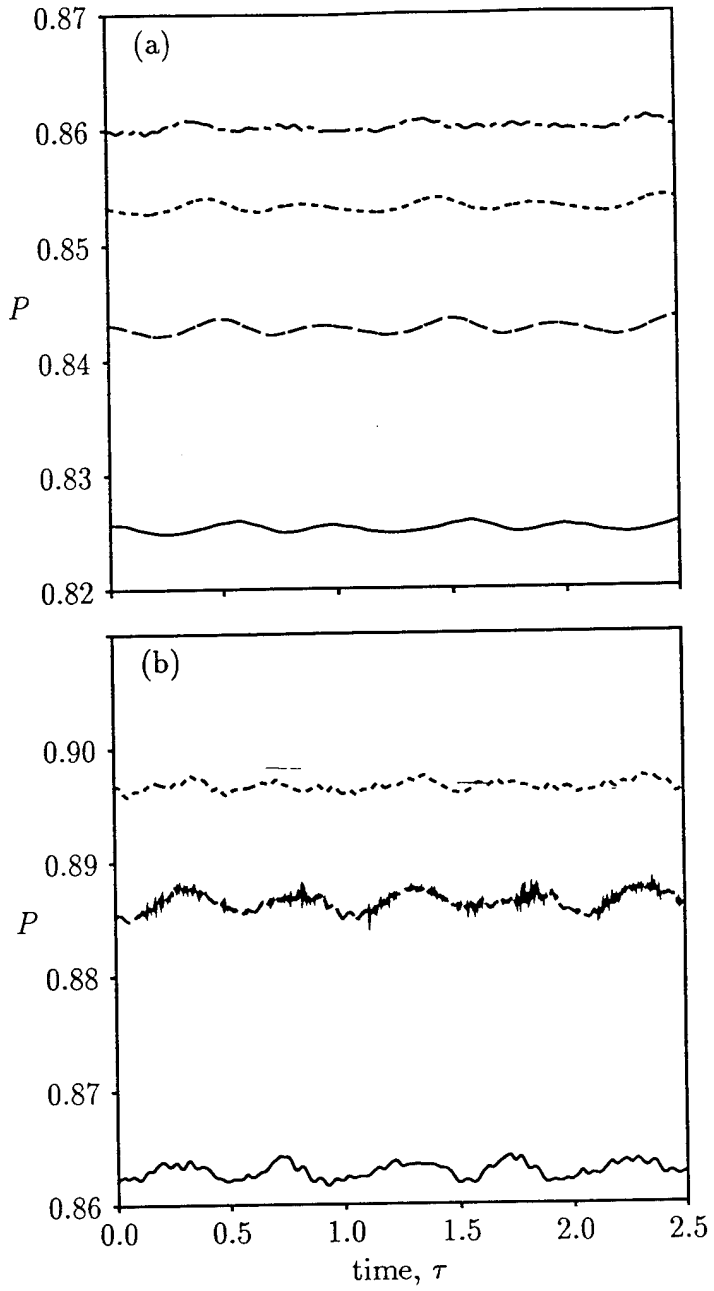

Figure 9: Surface-pressure time histories for flow in EGV cascade exposed to wakes with 30 percent velocity deficit at: (a) four upstream axial stations: ——: $s/s_{t.e.} \approx 0.100$, upstream of the time-averaged separation location; — — —: $s/s_{t.e.} \approx 0.129$, just upstream of the time-averaged separation location; - - - - -: $s/s_{t.e.} \approx 0.163$, about midway between the time-averaged separation point and the fixed transition location; — - — - —: $s/s_{t.e.} \approx 0.201$, just downstream of the start of transition, and upstream of the time-averaged reattachment location; (b) three downstream axial stations: ——: $s/s_{t.e.} \approx 0.217$, approximately midway between the start of transition and the time-averaged reattachment location; — — —: $s/s_{t.e.} \approx 0.237$, approximate time-averaged reattachment location; - - - - -: $s/s_{t.e.} \approx 0.260$, just downstream of the end of the fixed transition region.

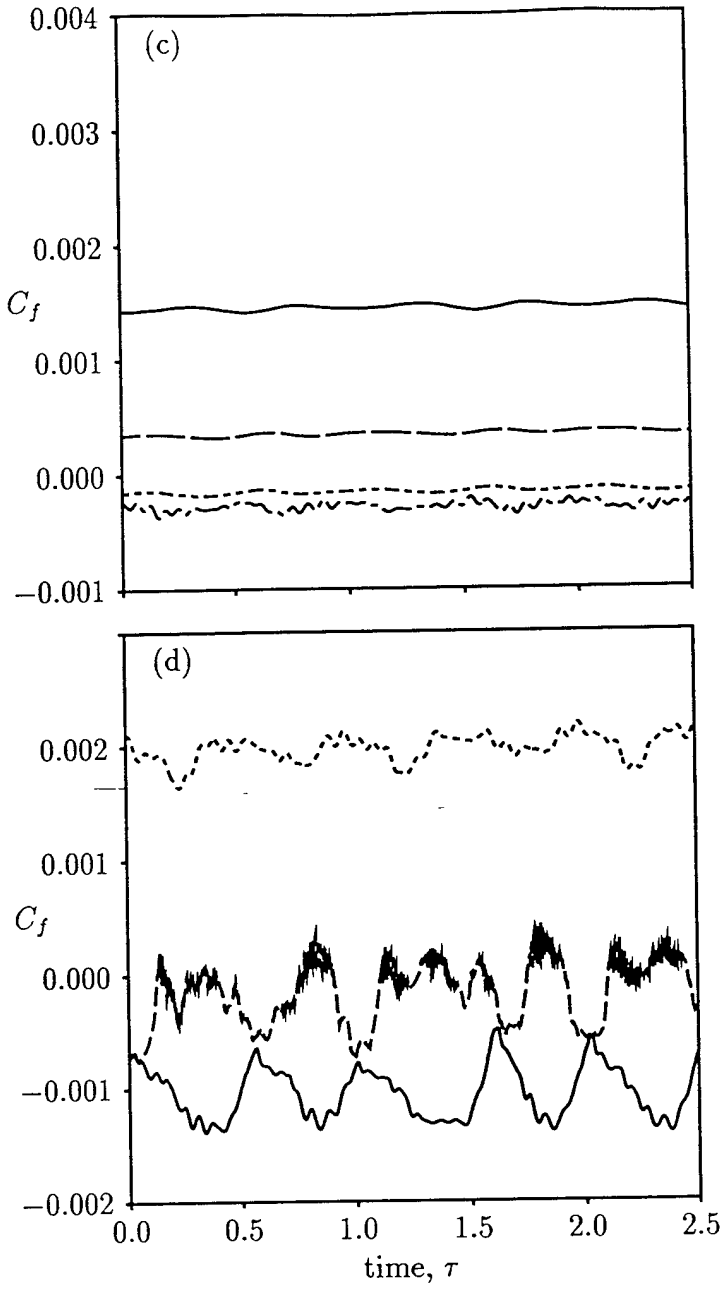

Figure 9: (continued) Surface shear stress time histories for flow in EGV cascade exposed to wakes with 30 percent velocity deficit at: (c) four upstream axial stations: ——: $s/s_{t.e.} \approx 0.100$, upstream of the time-averaged separation location; — — —: $s/s_{t.e.} \approx 0.129$, just upstream of the time-averaged separation location; - - - - -: $s/s_{t.e.} \approx 0.163$, about midway between the time-averaged separation point and the fixed transition location; — - — - — : $s/s_{t.e.} \approx 0.201$, just downstream of the start of transition, and upstream of the time-averaged reattachment location; (d) three downstream axial stations: ——: $s/s_{t.e.} \approx 0.217$, approximately midway between the start of transition and the time-averaged reattachment location; — — —: $s/s_{t.e.} \approx 0.237$, approximate time-averaged reattachment location; - - - - -: $s/s_{t.e.} \approx 0.260$, just downstream of the end of the fixed transition region.

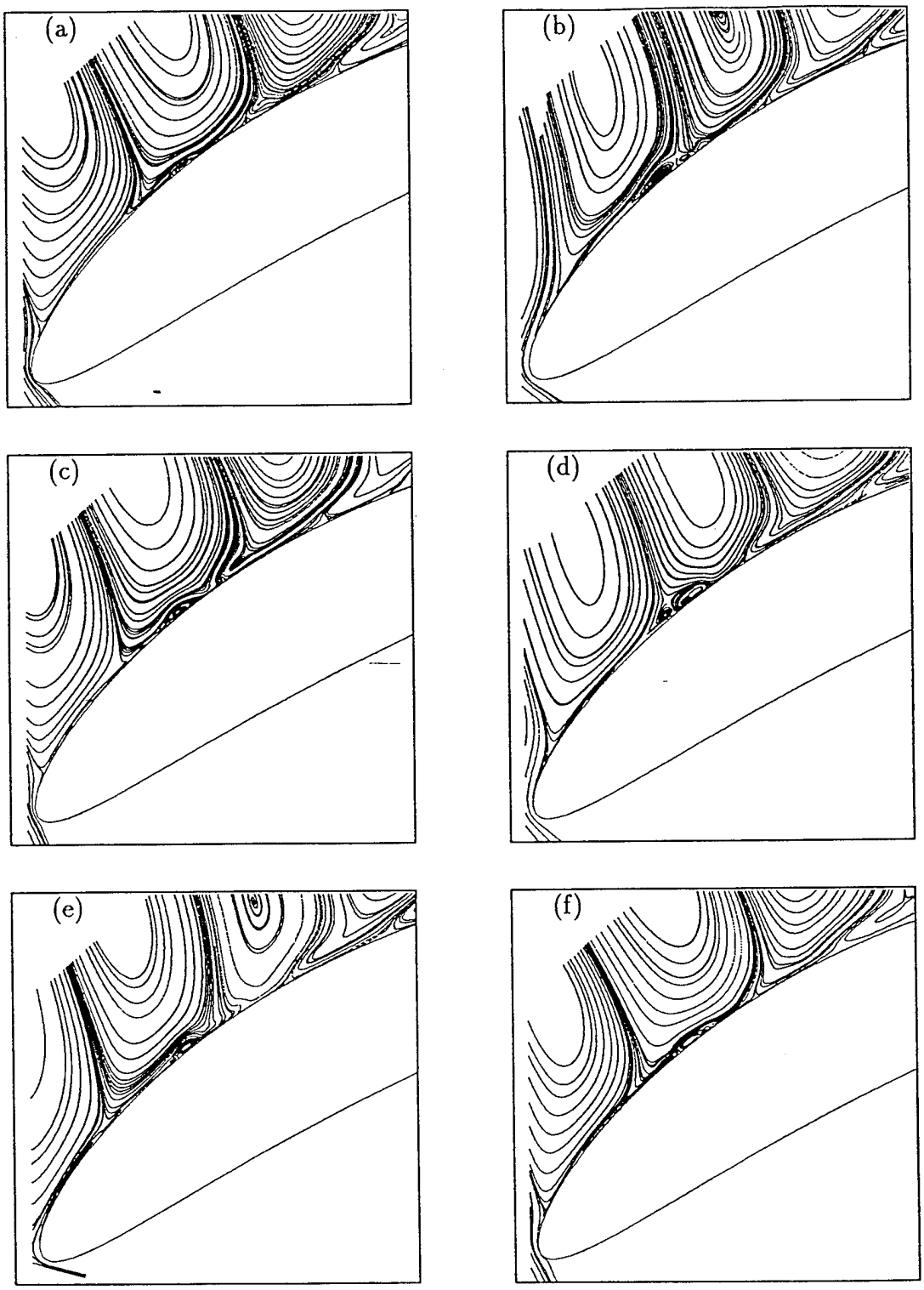

Figure 10: Instantaneous disturbance streakline patterns for EGV in presence of rotor wakes with 30 percent velocity deficit: (a) $T + 0T$; (b) $T + 0.2T$; (b) $T + 0.4T$; (b) $T + 0.6T$; (b) $T + 0.8T$; (b) $T + 1.0T$.

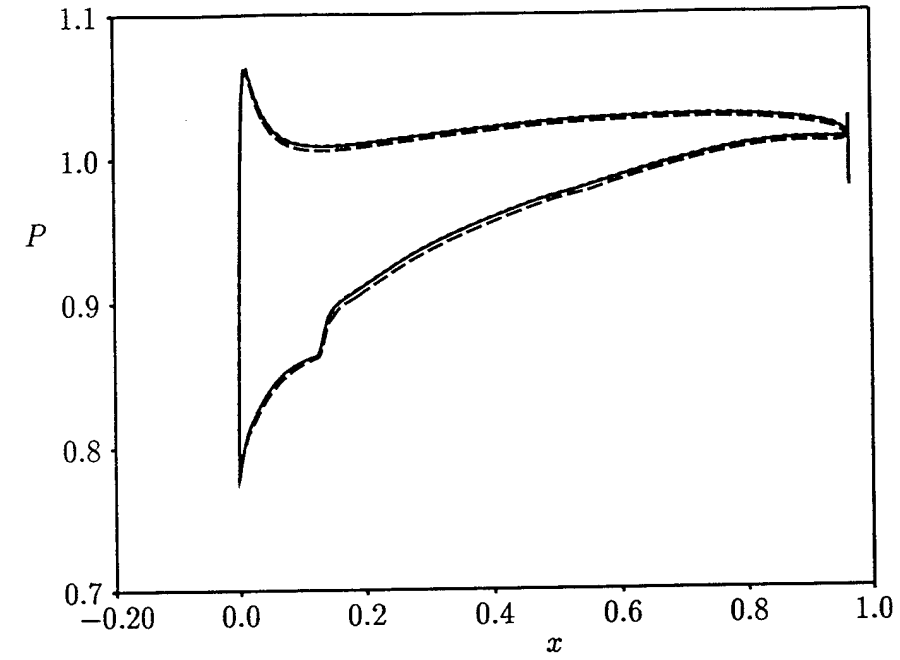

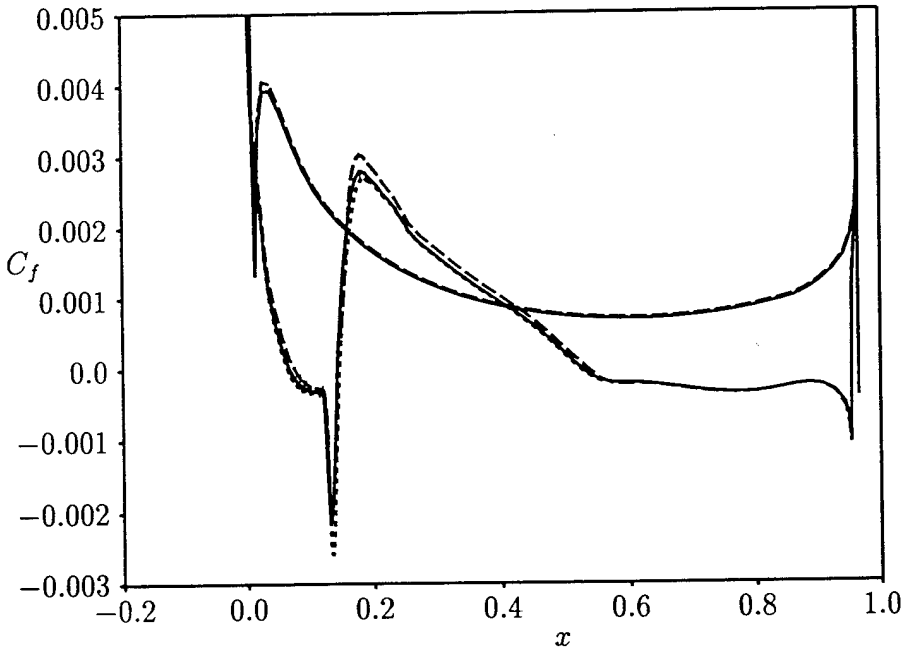

Figure 11: (a) Surface-pressure and (b) surface shear-stress distributions for EGV cascade: ———: undisturbed flow; - - - - - -: 5 percent wake deficit; — — —: 30 percent wake deficit.